JACS
JOURNAL OF THE AMERICAN CHEMICAL SOCIETY

ARTICLE

pubs.acs.org/JACS

Thermal Transformation of a Layered Multifunctional Network into a Metal−Organic Framework Based on a Polymeric Organic Linker

Patrícia Silva,[†] Fabiana Vieira,[†] Ana C. Gomes,[†] Duarte Ananias,[†] José A. Fernandes,[†] Sofia M. Bruno,[†] Rosário Soares,[‡] Anabela A. Valente,[†] João Rocha,[†] and Filipe A. Almeida Paz*[,†]

[†]Department of Chemistry and [‡]Central Analytical Laboratory, CICECO, University of Aveiro, 3810-193 Aveiro, Portugal

Supporting Information

ABSTRACT: The preparation of layered [La(H_3nmp)] as microcrystalline powders from optimized microwave-assisted synthesis or dynamic hydrothermal synthesis (i.e., with constant rotation of the autoclaves) from the reaction of nitrilotris(methylenephosphonic acid) (H_6nmp) with $LaCl_3 \cdot 7H_2O$ is reported. Thermogravimetry in conjunction with thermodiffractometry showed that the material undergoes a microcrystal-to-microcrystal phase transformation above 300 °C, being transformed into either a three-dimensional or a two-dimensional network (two models are proposed based on dislocation of molecular units) formulated as [La(L)] (where L^{3-} = $[-(PO_3CH_2)_2(NH)(CH_2PO_2)O_{1/2}-]_n^{3n-}$). The two crystal structures were solved from ab initio methods based on powder X-ray diffraction data in conjunction with structural information derived from ^{13}C and ^{31}P solid-state NMR, electron microscopy (SEM and EDS mapping), FT-IR spectroscopy, thermodiffractometry, and photoluminescence studies. It is shown that upon heating the coordinated H_3nmp^{3-} anionic organic ligand undergoes a polymerization (condensation) reaction to form in situ a novel and unprecedented one-dimensional polymeric organic ligand. The lanthanum oxide layers act, thus, simultaneously as insulating and templating two-dimensional scaffolds. A rationalization of the various steps involved in these transformations is provided for the two models. Photoluminescent materials, isotypical with both the as-prepared ([$(La_{0.95}Eu_{0.05})(H_3nmp)$] and [$(La_{0.95}Tb_{0.05})(H_3nmp)$]) and the calcined ([$(La_{0.95}Eu_{0.05})(L)$]) compounds and containing stoichiometric amounts of optically active lanthanide centers, have been prepared and their photoluminescent properties studied in detail. The lifetimes of Eu^{3+} vary between 2.04 ± 0.01 and 2.31 ± 0.01 ms (considering both ambient and low-temperature studies). [La(H_3nmp)] is shown to be an effective heterogeneous catalyst in the ring opening of styrene oxide with methanol or ethanol, producing 2-methoxy-2-phenylethanol or 2-ethoxy-2-phenylethanol, respectively, in quantitative yields in the temperature range 40−70 °C. The material exhibits excellent regioselectivity to the β-alkoxy alcohol products even in the presence of water. Catalyst recycling and leaching tests performed for [La(H_3nmp)] confirm the heterogeneous nature of the catalytic reaction. Catalytic activity may be attributed to structural defect sites. This assumption is somewhat supported by the much higher catalytic activity of [La(L)] in comparison to [La(H_3nmp)].

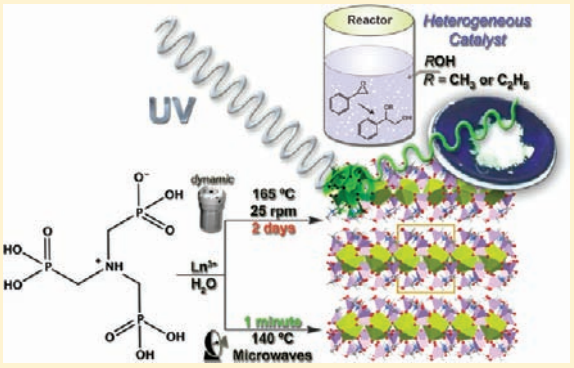

1. INTRODUCTION

Metal−Organic Frameworks (MOFs) and, in a more wide sense, coordination polymers remain nowadays one of the most studied topics in synthetic chemistry.[1] The field evolved considerably from the initial quest to design and isolate novel frameworks with unusual (and exotic) structural architectures[2] into the field of materials chemistry, sometimes with direct industrial applications.[3] Indeed, the unique combination into the same crystalline hybrid network of metal centers and organic molecules promotes the formation of compounds with interesting properties and structural features. For example, MOFs can now be employed as effective heterogeneous catalysts,[4] in the selective adsorption of gases,[5] as contrasting agents,[6] and in the fabrication of membranes[7] or thin films[8] and exhibit interesting photoluminescent properties,[9] enantioselective separation of molecules,[10] and magnetism.[11]

In the past few years, our research group has been particularly interested in the use of tripodal flexible organic molecules to construct multidimensional coordination polymers. Our strategy has been focused on the simultaneous replacement of carboxylic acid (CA) groups by phosphonic acid (PA) moieties and transition metal centers by rare-earth cations. Phosphonate moieties are interesting chelating moieties for the construction of MOFs[12] because while the three tetrahedral oxygen atoms mimic the building units of zeolites (thus providing various anchoring sites for a wide range of metals) they also induce the formation of networks with high thermal and mechanical robustness, which is an important prerequisite for possible applications (for example, catalytic activity at high temperatures).[13] Our aim

Received: June 7, 2011
Published: August 04, 2011

is to design more (mechanically and thermally) robust networks containing photoluminescent probes,[14] ultimately envisaging the potential fabrication of novel devices.[15] In this context, we have investigated several families of structures, all layered and based on: nitrilotriacetic acid (3 CA groups),[16] *N*-(phosphonomethyl)-iminodiacetic acid (2 CA and 1 PA groups),[17] (carboxymethyl)-iminodi(methylphosphonic acid) (1 CA and 2 PA),[18] and also nitrilotris(methylenephosphonic acid) (H_6nmp; 3 PA groups).[19] Surprisingly, the two latter organic molecules have been to date scarcely employed in the construction of multidimensional networks, either with *d*- or *f*-block elements.[19,20]

Following our recent motivation to explore faster and more efficient synthetic approaches with higher yields and smaller chemical waste, such as microwave heating,[21] in the present manuscript we report the isolation, full structural characterization, and heterogeneous catalytic activity of a novel layered material: [La(H_3nmp)]. We further demonstrate that the compound undergoes a microcrystal-to-microcrystal transformation (2D→3D or 2D→2D) with temperature, yielding an unprecedented compound with empirical formula [La(L)] (where L^{3-} = $[-(PO_3CH_2)_2(NH)(CH_2PO_2)O_{1/2}-]_n^{3n-}$). Noteworthy, this latter compound is obtained by the in situ condensation of residues of H_6nmp, leading to the formation of a one-dimensional (i.e., infinite) organic ligand. To the best of our knowledge, this type of ligand transformation, which also leads to a (poorly) crystalline material, has never been reported to date. Optical centers, in particular Eu^{3+}, have been engineered into the frameworks of [La(H_3nmp)] and [La(L)] to produce photoluminescent materials with lifetimes above 2 ms. We further explore the use of [La(H_3nmp)] and [La(L)] as a heterogeneous catalysts in the ring opening of styrene oxide. Epoxide ring-opening reactions with alcohols are an important transformation in the synthesis of β-alkoxy alcohols, which can be employed as valuable organic solvents, natural products, or intermediates, in organic and inorganic synthesis.[22] Noteworthy, early ring-opening reactions resulted in polymerization and low selectivity because of the required high temperatures. We show in this work that both the layered and the MOF materials are highly regioselective catalysts in the conversion of styrene oxide into 2-methoxy-2-phenylethanol (or 2-ethoxy-2-phenylethanol) by epoxide ring opening with methanol (or ethanol) under relatively mild reaction conditions. It is further shown that the catalytic reaction is heterogeneous in nature, and the active sites may be structural defects. The MOF compound [La(L)] revealed excellent regioselectivity, similar to [La(H_3nmp)], and the catalytic activity was much higher.

2. RESULTS AND DISCUSSION

2.1. Structural Design and Synthesis Strategy. Our main objective focuses on the preparation of compounds topologically similar to the layered [La(H_3nmp)]·1.5H_2O network[19] while using a faster, simpler, and also environmentally more friendly synthetic procedure, thus envisaging future potential applications in the fabrication of functional materials. Microwave-assisted heating can address some of these requirements.[21] Because the experimental conditions cannot be directly transposed from conventional hydrothermal synthesis into microwave-assisted synthesis (even though a relatively identical composition for the reactive system was indeed used—see dedicated Materials and Methods), a systematic variation of the experimental variables to obtain (i) phase-pure and (ii) highly crystalline materials while (iii) exhibiting uniform crystal habit and size distribution had to be performed (results in the following subsection).

Scheme 1. $T_mP_nt_p$ Diagram for the Optimization of the Microwave-Assisted Hydrothermal Synthesis of [La(H_3nmp)] (1)[a]

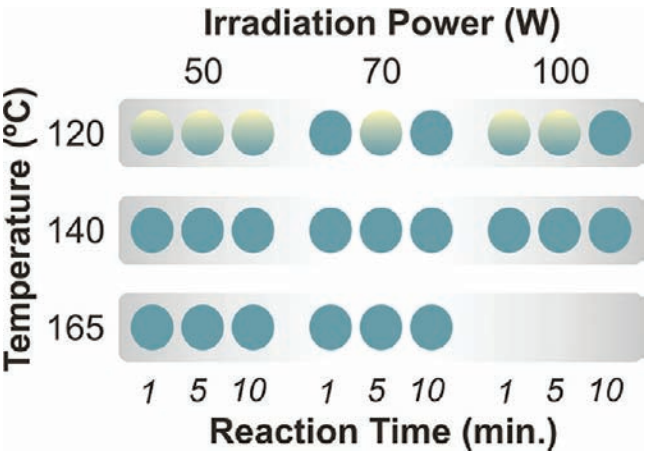

[a] Legend: solid blue circle, phase-pure **1**; shaded circle, mixture of **1** with other phases, which include [La(H_3nmp)]·1.5H_2O or other unknown materials.

As for related systems, these materials are likely to be isolated as microcrystalline powders. La^{3+} was therefore selected as the pivot metallic node because: (i) it promotes diamagnetic networks which can be studied using solid-state NMR techniques (to derive information on the composition of the asymmetric unit) and (ii) it is of great usefulness to prepare a nonemitting (in the visible region) hybrid matrix which can be doped with stoichiometric amounts of emitting lanthanide centers such as Tb^{3+} and Eu^{3+}. In addition, small percentages of these optically active metal centers can also boost the observed photoluminescent properties by reducing self-quenching effects.

2.1.1. Microwave-Assisted Hydrothermal Synthesis: Optimization. The optimization process covered a wide range of experimental conditions (see Materials and Methods for details). Several compounds have been prepared (Scheme 1) and inspected using, mainly, a combination of powder X-ray diffraction and electron microscopy (SEM imaging and EDS analyses).

Phase-pure [La(H_3nmp)] (**1**) can be isolated over a wide range of experimental conditions. At 120 °C, mixtures of **1** with other phases, either known or unknown, are mainly observed. Considering that mild and faster experimental conditions are usually preferred, 140 °C arises as the optimal minimum temperature to isolate **1**, independently of either the power of the irradiation or the time of reaction employed.

2.1.2. Crystal Morphology. Crystal morphology and average particle size vary slightly according to the selected reaction conditions. Crystals of **1** exhibit similar platelike morphology for a wide range of conditions with individual crystallites being stacked into different types of aggregates, such as flower- and bone-like ones (Figure 1a). Crystals are, thus, very regular thin (in the nanometer range) plates which grow uniformly without the presence of precipitates (or other defects) in the matrix. This was clearly observed using TEM studies (Figure 1b). Because of the sensitivity of **1** toward the electron beam (most likely due to the presence of the organic component), more detailed high-resolution TEM studies could not be performed.

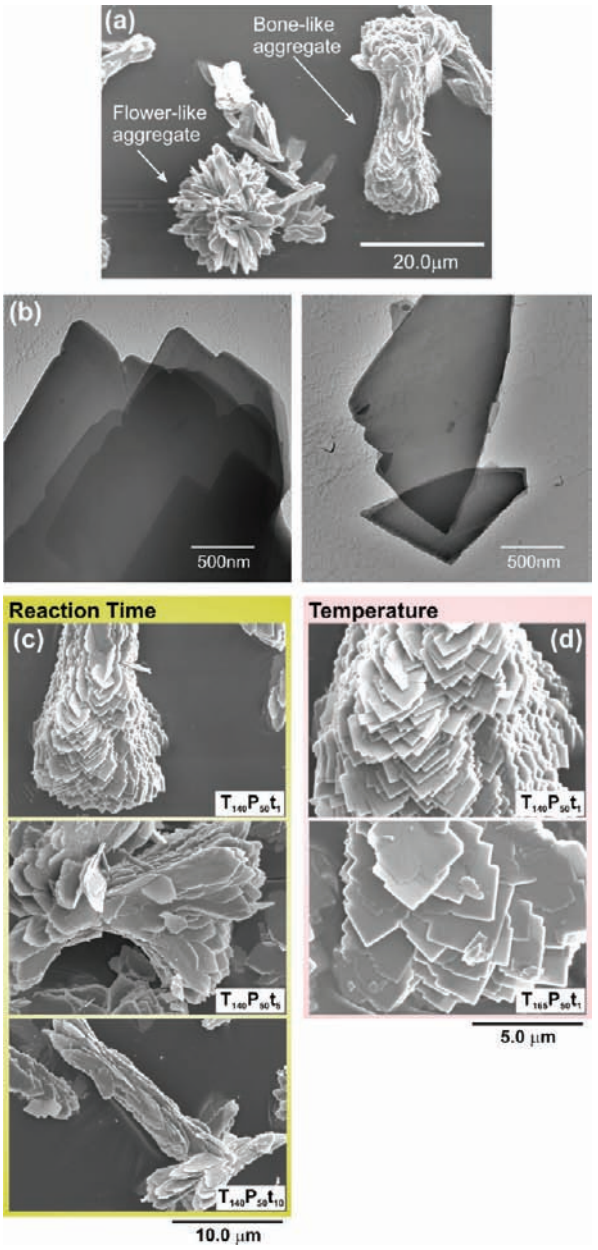

Figure 1. (a) SEM image of [La(H$_3$nmp)] (**1**−$T_{140}P_{50}t_1$) showing the two main different types of crystallite aggregates isolated directly from the reaction vessel. (b) TEM images (bright field) of **1**−$T_{140}P_{50}t_1$ depicting the nanosized thickness and homogeneity of the crystallites. Effect on the crystallite morphology and size when varying (c) the reaction time and (d) the temperature.

On average, the increase of the reaction time of the microwave-assisted synthesis is concomitant with an average increase of the particle size, even though smaller crystals can also be isolated for longer periods of irradiation (see, for example, the SEM picture of the material **1**-$T_{140}P_{50}t_{10}$, Figure 1c below). This effect can also be promoted by the fact that long microwave irradiation periods are also known to lead to the partial destruction of the prepared compounds, as reported for other MOF-type materials.[23]

Distinct irradiation powers do not seem to produce significant changes in either the size or the shape of the crystallites (data not shown). Conversely, an increase of the temperature of reaction has a

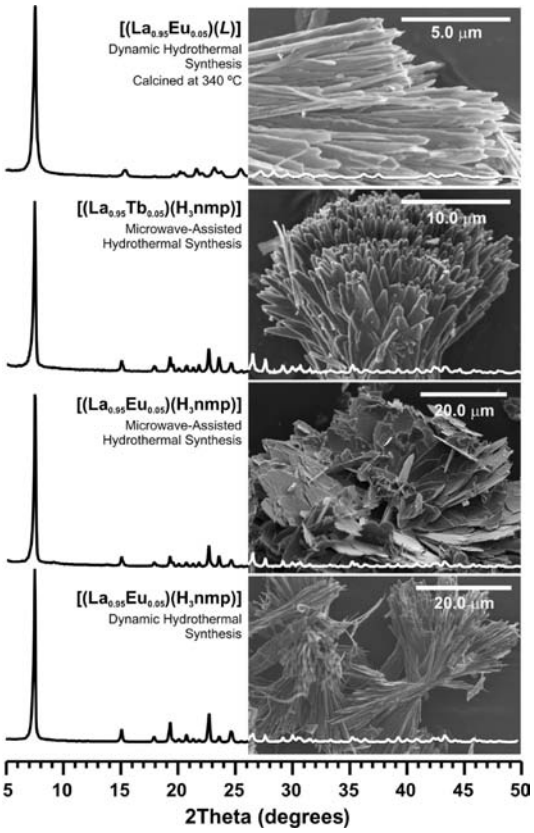

Figure 2. Powder X-ray diffraction patterns and SEM images of the bulk materials with stoichiometric amounts of Eu^{3+} and Tb^{3+} lanthanide centers and prepared using either microwave-assisted synthesis or dynamic hydrothermal synthesis.

pronounced effect on particle dimension as noticeable in Figure 1d when comparing samples **1**−$T_{140}P_{50}t_1$ and **1**−$T_{165}P_{50}t_1$.

2.1.3. Dynamic Hydrothermal Synthesis of [La(H$_3$nmp)]. Under comparable synthetic conditions (i.e., temperature and chemical composition of the reactive mixtures), [La(H$_3$nmp)] (**1**) cannot be prepared using typical static hydrothermal synthesis: a mixture of [La(H$_3$nmp)]·1.5H$_2$O and a novel, poorly crystalline and unidentified phase is always isolated. We envisaged that stirring during the synthesis (as it occurs in the microwave-assisted method) could be a key experimental factor for the successful preparation of **1**. By employing experimental conditions relatively similar to those optimized for the microwave-assisted synthesis, **1** was isolated in just 48 h of reaction when the reaction vessel was kept under constant rotation at 165 °C. Noteworthy, the optimal frequency of rotation was found to be 25 rpm.

2.1.4. Engineering Optical Centers into the Materials. Optically active compounds containing stoichiometric amounts of Eu^{3+} or Tb^{3+} were isolated as microcrystalline [(La$_{0.95}$Eu$_{0.05}$)(H$_3$nmp)] and [(La$_{0.95}$Tb$_{0.05}$)(H$_3$nmp)] bulk materials, with only small differences in crystallite size and morphology being observed (see SEM pictures in Figure 2). As registered for the parent [La(H$_3$nmp)] (**1**) material, photoluminescent [(La$_{0.95}$Eu$_{0.05}$)(L)] (where L^{3-} = $[-(PO_3CH_2)_2(NH)(CH_2PO_2)O_{1/2}-]_n^{3n-}$) can also be readily prepared by calcination of the mixed-lanthanide [(La$_{0.95}$Eu$_{0.05}$)(H$_3$nmp)] compound (Figure 2, top). EDS mapping studies (Figures S1−S5 in the Supporting Information in the ESI) clearly show that: (i) Eu^{3+} and Tb^{3+} centers were incorporated

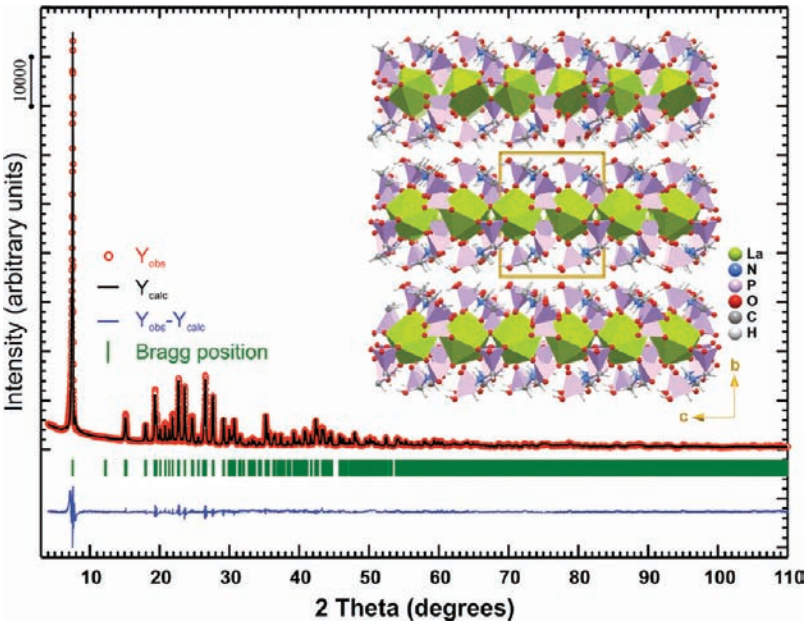

Figure 3. Final Rietveld plot (powder X-ray diffraction data) of [La(H_3nmp)] (**1**). Observed data points are indicated as red circles, and the best-fit profile (upper trace) and the difference pattern (lower trace) are drawn as solid black and blue lines, respectively. Green vertical bars indicate the angular positions of the allowed Bragg reflections. Refinement details are given in Table 1. Inset: Crystal packing of **1** viewed in perspective along the [100] direction of the unit cell.

into the prepared networks; (ii) the distribution of these elements is completely random inside the crystallites; (iii) the inclusion of these optical centers occurs in an identical fashion using either microwave-assisted synthesis or dynamic hydrothermal synthesis.

2.2. Crystal Structure Elucidation and Description of [La(H_3nmp)] (1). Materials produced using either microwave-assisted hydrothermal synthesis or the dynamic hydrothermal approach are systematically isolated as microcrystalline powders, which prevented a priori a straightforward structural elucidation from single-crystal X-ray diffraction studies. As in our previous study on the [La(H_3nmp)]·1.5H_2O and [Ln(H_2cmp)(H_2O)] [Ln^{3+} = Y^{3+}, La^{3+}, Pr^{3+}, Nd^{3+}, Sm^{3+}, Eu^{3+}, Gd^{3+}, Tb^{3+}, Dy^{3+}, Ho^{3+}, and Er^{3+}; H_5cmp = *N*-(carboxymethyl)iminodi(methylphosphonic acid)] materials,[18b] solid-state NMR studies provided fundamental data on the composition of the asymmetric unit: the ^{31}P MAS spectrum of **1** shows the presence of three well-resolved isotropic resonances in the −8 to 14 ppm spectral region (Figure S7 in the Supporting Information); the $^{13}C\{^1H\}$ CP MAS spectrum further revealed the existence of six resonances, grouped into three pairs of peaks separated by ca. 126−133 Hz (within experimental error; Figure S6 in the Supporting Information), which is consistent with the existence of spin multiplets arising from $^1J_{C,P}$ coupling (usually in the 5−90 Hz range).[24] In summary, this technique clearly supports the existence of a single crystallographically unique $H_{6-x}nmp^{-x}$ residue in the asymmetric unit. Additionally, and based on the performed photoluminescence studies (see dedicated section below), the material should also contain a single independent lanthanide center.

The crystal structure of [La(H_3nmp)] (**1**) was unveiled from ab initio X-ray powder studies (Figure 3). The material crystallizes in the noncentrosymmetric orthorhombic $Pca2_1$ space group (Table 1), with the composition of the asymmetric unit being in good agreement with the assumptions highlighted above. The single La^{3+} center is nine-coordinated, {LaO_9}, to a total of seven phosphonate groups arising from four symmetry-related H_3nmp^{3-} anionic ligands, with the coordination polyhedron resembling a highly distorted tricapped trigonal prism as depicted in Figure 4b. The La−O bond lengths were found in the 2.487(12)−2.932(11) Å range (Table 2). We note that the latter, relatively long bond length is directly associated with the P1 phosphonate group which is deeply embedded inside the lanthanum oxide layer, establishing physical connections between four adjacent La^{3+} cations (see Figures S11a and S11b in the Supporting Information for detailed views). This type of behavior has already been reported for [Pr(H_3nmp)]·1.5H_2O but with a slightly distinct coordination mode: while in **1** the P1 phosphonate group is *O*,*O*-chelated to two La^{3+} cations, in the Pr^{3+}-containing material this type of chelation only occurs to one neighboring metal center; this also seems to be the structural reason for the existence of a nine-coordination geometry in the present material, contrasting with the eight-coordinated dodecahedral environment of our previous structure.[19] While in [Pr(H_3nmp)]·1.5H_2O the layer arrangement was mainly based on the presence of a 1D chain of Pr^{3+} polyhedra, in **1** the distribution of the metallic centers within the layer is significantly more uniform (as shown in Figure 4a) with the intermetallic La···La distances varying only between ca. 4.59 and 4.82 Å (for reference, in [Pr(H_3nmp)]·1.5H_2O the intralayer Pr···Pr distances varied instead between ca. 4.24 and 5.89 Å).

Another striking distinction between **1** and [Pr(H_3nmp)]·1.5H_2O concerns the connectivity among adjacent lanthanide polyhedra: in the latter compound layers are based on 1D chains formed by edge-shared Pr^{3+} polyhedra, further interconnected via a phosphonate group to yield the layer; in **1**, each La^{3+} polyhedron is connected instead to another four via corner sharing, leading to a significantly more dense structure (Figure 4a). This connectivity in **1** seems to be the main driving force for the existence of an almost planar and infinite lanthanum oxide layer (inset in Figure 3), while in [Pr(H_3nmp)]·1.5H_2O the phosphonate bridge induces flexibility, ultimately promoting a kink in the layer and an empty space within the crystal structure filled with uncoordinated water molecules.

Table 1. X-ray Data Collection, Crystal Data, and Structure Refinement Details for [La(H$_3$nmp)] (1) and the Two Models for [La(*L*)] (2) (where L^{3-} = $[-(PO_3CH_2)_2(NH)(CH_2PO_2)O_{1/2}-]_n^{3n-}$)

	1	2 (model I)	2 (model II)
Unit Cell			
formula	$C_3H_9LaNO_9P_3$	$C_3H_7LaNO_8P_3$	$C_3H_7LaNO_8P_3$
formula weight	434.93	416.92	416.92
crystal system	orthorhombic	orthorhombic	orthorhombic
space group	$Pca2_1$	$Pca2_1$	$Pca2_1$
a/Å	9.1762(3)	9.7660(6)	8.7247(5)
b/Å	11.7369(4)	11.3438(3)	11.3493(3)
c/Å	9.8340(3)	8.7307(5)	9.7728(6)
volume/Å^3	1059.12(6)	967.21(8)	967.69(8)
Z	4	4	4
D_c/g cm^{-3}	2.728	2.863	2.863
Profile Parameters			
profile function	pseudo-Voigt	Thompson−Cox−Hastings pseudo-Voigt	Thompson−Cox−Hastings pseudo-Voigt
Caglioti law parameters (for **1**)	U = 0.115(6)	Y00 = 3.48(6);	Y00 = 3.44(5);
spherical harmonics for size broadening	V = −0.079(3)	Y20 = −1.7(1);	Y20 = 0.4(1);
	W = 0.0263(4)	Y22+ = −0.8(1);	Y22+ = −0.85(8);
orthorhombic crystal system (for **2**)		Y40 = −0.9(1);	Y40 = −0.6(1);
		Y42+ = −1.84(8);	Y42+ = −0.09(7);
		Y44+ = 0.71(9)	Y44+ = 0.20(7)
asymmetry parameters (up to 20° 2θ)	0.0343(7) and 0.0218(2)	0.0183(4) and 0.0036(1)	0.0162(3) and 0.0038(1)
zero shift [2θ°]	−0.0159(8)	−	−
Refinement Details			
no. of independent reflections	653	516	512
no. of global refined parameters	1	0	0
no. of profile refined parameters	9	13	13
no. of intensity-dependent refined parameters	56	52	52
Reliability Factors for All Nonexcluded Data Points with Bragg Contribution (Conventional—Not Corrected for Background)			
R_p	7.15	5.14	4.33
R_{wp}	9.78	6.81	5.61
R_{exp}	2.38	6.52	6.51
χ^2	17.5	1.09	0.74
Structure Reliability Factors			
R_{Bragg}	9.58	7.90	6.93
R_F	14.7	20.0	19.0
Indexing Figures-of-Merit			
M(n)	44.3 (n = 20)	14.3 (n = 19)	14.3 (n = 19)
F(n)	66.3 (n = 20)	19.0 (n = 19)	19.0 (n = 19)

The {LaO_9} coordination polyhedron of **1** is water-free (as observed in [Pr(H$_3$nmp)]·1.5H$_2$O), and the material itself does not contain water. Consequently, the interlayer bridges based on O−H···O hydrogen bonds reported for [Pr(H$_3$nmp)]·1.5H$_2$O are completely absent in **1**. The protonated phosphonate groups are instead engaged in strong hydrogen bonding interactions which cover the outer shell of the two-dimensional layers as depicted in Figure 4a. Individual layers pack in a parallel fashion along the [010] direction of the unit cell, leading to the crystal structure depicted as an inset in Figure 3.

2.3. Thermogravimetry and Thermodiffractometry. The thermal behavior of the bulk layered [La(H$_3$nmp)] (**1**) material was investigated between ambient temperature and ca. 800 °C (Figure 5). Thermogravimetric analysis in conjunction with thermodiffractometry clearly shows that the overall crystalline structure of the material remains intact up to ca. 280 °C. A small continuous weight drop registered between ca. 200 and 250 °C is mainly attributed to physisorbed and chemisorbed water molecules arising from local structural defects because, as described above, **1** does not contain any water molecules in its crystal structure composition. Between 250 and 400 °C the material undergoes a crystalline phase transition with the first reflection (corresponding to the (010) plane) being shifted to higher 2θ values while getting significantly broader. This shift points to a reduction of the unit cell dimensions, in particular along the [010] direction, which further indicates a closer proximity

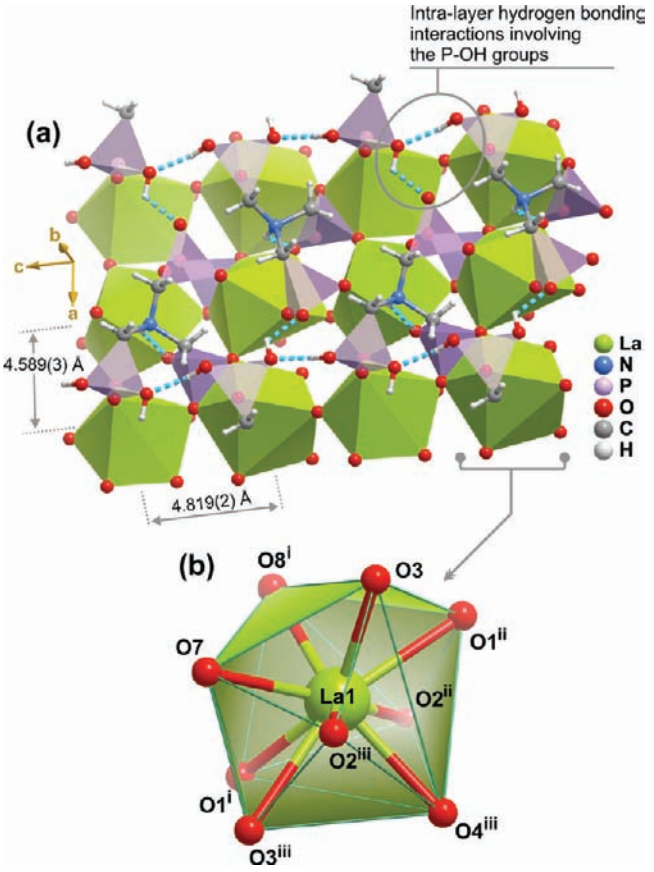

Figure 4. (a) Schematic representation of a portion of the two-dimensional network of [La(H_3nmp)] emphasizing the connectivity of the H_3nmp^{3-} organic residues to the lanthanum oxide core. Intralayer hydrogen bonding interactions are represented as blue-filled dashed lines (symmetry codes have been omitted for clarity): N1−H1C···O3 with $d_{D\cdots A}$ = 2.823(13) Å and <(DHA) of ca. 128°; O5−H5A···O9 with $d_{D\cdots A}$ = 2.328(15) Å and <(DHA) of ca. 126°; O6−H6A···O5 with $d_{D\cdots A}$ = 2.720(15) Å and <(DHA) of ca. 170°. (b) Highly distorted {LaO_9} tricapped trigonal prismatic coordination environment of La^{3+}. For selected bond lengths (in Å) and angles (in degrees), see Table 2. Symmetry transformations used to generate equivalent atoms: (i) 1/2 − *x*, *y*, 1/2 + *z*; (ii) 1 − *x*, 1 − *y*, 1/2 + *z*; (iii) −1/2 + *x*, −*y*, *z*.

between lanthanum oxide layers. Indeed, in the 250−400 °C temperature window the compound loses approximately 4.2% of total weight, which agrees well with the release of one water molecule per formula unit (calculated of about 4.1%). We note that this occurrence is coherent with the observed structural transformation described in the following subsection. Above 400 °C additional weight losses are attributed to the full decomposition of the organic component, with thermodiffractometry indicating the existence of an almost amorphous compound. At 680 °C the residue was identified (PDF4-release 2010 database) as a crystalline mixture composed of monazite ($LaPO_4$, ICDD 00-032-0493) and lanthanum catenatriphosphate (LaP_3O_9, ICDD 01-084-1635).

A representative portion of the [La(L)] (**2**) material (where L^{3-} = $[-(PO_3CH_2)_2(NH)(CH_2PO_2)O_{1/2}-]_n^{3n-}$) was isolated by calcining the parent compound **1** at 340 °C for ca. 3 h. As already suggested by the previous studies, the slow heating of **2** promotes a continuous release of mass over the wide

Table 2. Bond Lengths (in Å) and Angles (in Degrees) for the La^{3+} Coordination Environment in [La(H_3nmp)] (1)[a]

La1−O1^{i}	2.487(12)	La1−O3^{iii}	2.932(11)
La1−O1^{ii}	2.706(12)	La1−O4^{iii}	2.634(8)
La1−O2^{iii}	2.501(15)	La1−O7	2.503(11)
La1−O2^{ii}	2.671(15)	La1−O8^{i}	2.601(11)
La1−O3	2.518(11)		
O1^{ii}−La1−O1^{i}	128.6(5)	O2^{iii}−La1−O3	71.4(6)
O1^{i}−La1−O2^{ii}	76.1(6)	O2^{iii}−La1−O3^{iii}	54.5(5)
O1^{i}−La1−O2^{iii}	113.0(6)	O2^{ii}−La1−O4^{iii}	70.5(6)
O1^{ii}−La1−O2^{ii}	55.1(6)	O2^{iii}−La1−O4^{iii}	77.4(5)
O1^{ii}−La1−O2^{iii}	116.7(6)	O2^{ii}−La1−O7	142.8(5)
O1^{i}−La1−O3	151.4(5)	O2^{iii}−La1−O7	67.2(6)
O1^{i}−La1−O3^{iii}	59.1(5)	O2^{ii}−La1−O8^{i}	78.9(5)
O1^{ii}−La1−O3^{iii}	158.9(5)	O2^{iii}−La1−O8^{i}	132.60(4)
O1^{ii}−La1−O3	62.1(5)	O3−La1−O3^{iii}	122.3(5)
O1^{i}−La1−O4^{iii}	96.1(5)	O3−La1−O4^{iii}	112.2(5)
O1^{ii}−La1−O4^{iii}	82.8(5)	O3^{iii}−La1−O4^{iii}	76.5(5)
O1^{i}−La1−O7	74.9(5)	O3−La1−O7	81.7(5)
O1^{ii}−La1−O7	136.9(5)	O3^{iii}−La1−O7	61.3(5)
O1^{i}−La1−O8^{i}	79.3(5)	O3−La1−O8^{i}	78.3(5)
O1^{ii}−La1−O8^{i}	76.9(4)	O3^{iii}−La1−O8^{i}	123.8(5)
O2^{iii}−La1−O2^{ii}	147.5(5)	O4^{iii}−La1−O7	135.4(5)
O2^{ii}−La1−O3	116.4(6)	O4^{iii}−La1−O8^{i}	149.2(5)
O2^{ii}−La1−O3^{iii}	119.9(6)	O7−La1−O8^{i}	73.3(5)

[a] Symmetry transformations used to generate equivalent atoms: (i) 1/2 − *x*, *y*, 1/2 + *z*; (ii) 1 − *x*, 1 − *y*, 1/2 + *z*; (iii) −1/2 + *x*, −*y*, *z*.

temperature range 25−800 °C as depicted in Figure S9 (in the Supporting Information). Despite the several (and discernible) consecutive weight losses, it is not possible to unequivocally identify which molecular entities are being released at one given temperature. It is, however, possible to observe that the residue reminiscent at ca. 800 °C agrees well with the stoichiometric formation of the inorganic residue LaP_3O_8 (by assuming a change of the oxidation state of one phosphorus from +5 to +3). This result indicates the complete transformation of the material into an inorganic phase, which is in agreement with the TGA results previously discussed for **1**.

2.4. Crystal Structure Elucidation and Description of [La(L)] (2). The crystalline material isolated in the ca. 300−400 °C temperature range was studied using ^{31}P solid-state NMR (Figure S8 in the Supporting Information). Three sharp resonances peaking at ca. −7.1, −3.3, and 10.5 ppm remain indicative of the presence of three distinct crystallographic sites for phosphorus, coherent with the previous results for [La(H_3nmp)] (**1**), still supporting the existence of a single crystallographically independent $H_{6-x}nmp^{-x}$ residue in the asymmetric unit of the newly formed compound. The observed chemical shifts are slightly distinct from those registered for **1** (ca. −3.6, 3.2, and 8.4 ppm; Figure S7 in the Supporting Information), indicating that the local environments of the phosphorus atoms were modified in the process. We further note the presence of a very broad resonance centered at about −26.4 ppm, typical of purely inorganic compounds,[25] with its large full-width-at-half-maximum (fwhm) indicating an amorphous phase. Photoluminescence studies (see below) also indicate the existence of such phase, which already seems to exist in the parent [La(H_3nmp)] (**1**) compound even though it passes undetected using most of the characterization techniques. This secondary

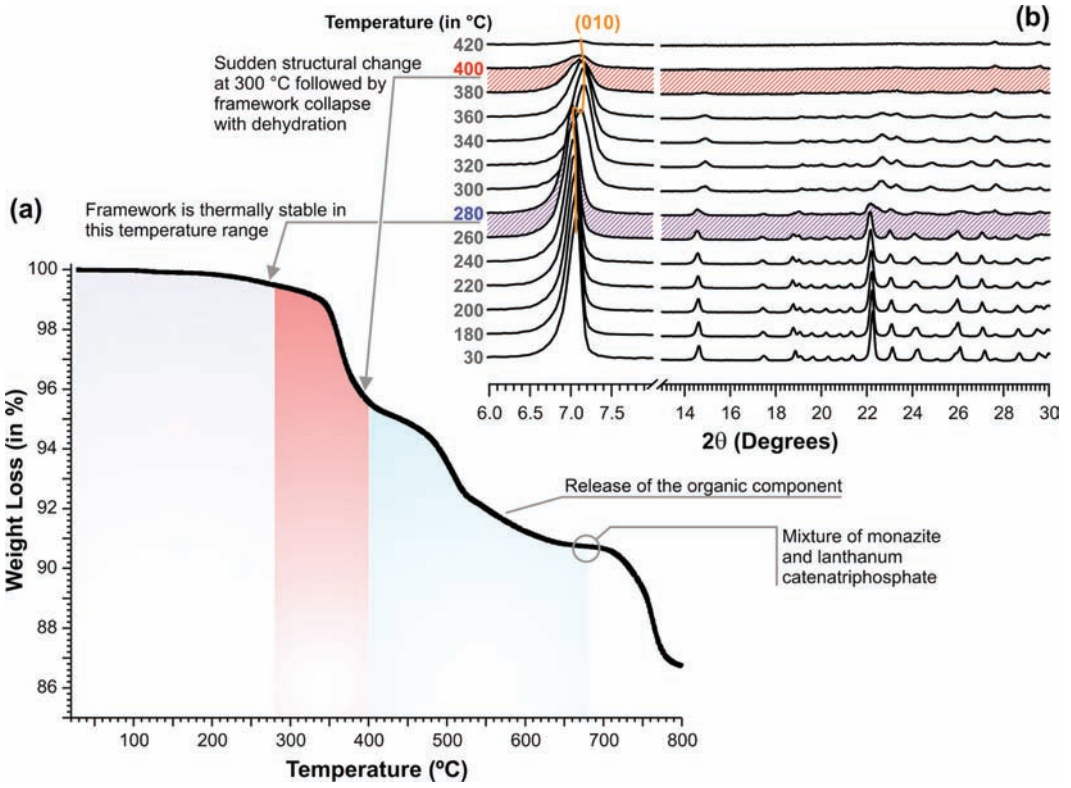

Figure 5. Thermogram and variable-temperature powder X-ray diffraction studies of [La(H_3nmp)].

inorganic phase seems to contain a small amount of protons because the resonance is significantly less visible in the $^{31}P\{^1H\}$ CP MAS spectrum (Figure S8 in the Supporting Information).

As in the parent material **1**, and despite the considerable decrease in overall crystallinity, structural models for the structure of the calcined material were derived from powder X-ray diffraction data (Figure 6). The material was formulated as [La(L)] (**2**) (where $L^{3-} = [-(PO_3CH_2)_2(NH)(CH_2PO_2)O_{1/2}-]_n^{3n-}$), which depending on the model (I or II) could be either a 2D or a 3D network. Electron microscopy imaging shows that the overall crystal morphology is not significantly affected by the thermal treatment (see, for example, Figure 2 at the top and the inset in Figure 6). We thus infer that the observed reduction of crystallinity must then occur within the crystallites, as observed from the TEM studies at the nanolevel depicted in Figure S22 in the Supporting Information: the crystals contain holes and nanodomains with distinct contrast. The most remarkable structural feature of **2**, indicated by either of the derived models, concerns the existence of a one-dimensional infinite organic ligand (see the following section for additional details) either decorating or pillaring the lanthanum oxide layers reminiscent from the parent compound (Figure 7). In model I, this polymeric organic linker runs parallel to the [100] crystallographic direction, in a wavelike fashion with a period of the length of the *a*-axis of the unit cell. Conversely, in model II the same polymeric organic linker is parallel to the [001] direction (period of the *c*-axis).

Independently of the model for **2**, upon thermal treatment the coordination environment of the crystallographically independent La^{3+} center changes considerably as depicted in Figure 8. On one hand, the coordination number is reduced to eight in both models, $\{LaO_8\}$, because the metal center is now only coordinated to a total of six phosphonate moieties due to the rupture of one La−O bond to form the polymeric ligand (details in subsection 2.7). The resulting highly distorted square antiprismatic (model I) or bicapped trigonal prismatic (model II) coordination environments have, in average, significantly longer La−O bond lengths when compared to **1**: found in the 2.647(9)−2.823(9) Å and 2.543(10)−2.657(9) Å ranges (Tables 3 and 4). While the P1 phosphonate group remains strongly *O*,*O*-chelated to two neighboring La^{3+} cations as in **1**, the two remaining phosphonate moieties modify considerably their environment in the two models: in model I, while one group establishes a new μ_2-bridge between adjacent cations, the other does not interact with any metal center being instead involved in the formation of the pyrophosphonate bridge (P···P distance of about 2.95 Å); in model II, both groups are interacting with an adjacent La^{3+} cation as depicted in Figure S13 in the Supporting Information. This transformation induces, for the two models, small changes in the lanthanum oxide layer, with adjacent $\{LaO_8\}$ polyhedra being edge-shared which ultimately leads to closer intermetallic distances as depicted in Figure 8.

2.5. Vibrational Spectroscopy. Vibrational FT-IR spectroscopy studies support, on the one hand, the highlighted structural features of [La(H_3nmp)] (**1**) and, on the other, that it is highly sensitive to the structural transformation that leads to the formation of [La(L)] (**2**).[26] Figure 9 focuses on the ca. 1500−700 spectral region of the FT-IR spectra of **1** and **2**, including assignments for each main observed band. We note that the most relevant differences were clearly observed in this region, which corresponds to that where the various vibrational modes of P−O groups appear. A representation of the progressive modification of selected spectral regions with increasing temperature (i.e., when going from compound **1** to **2** by thermal

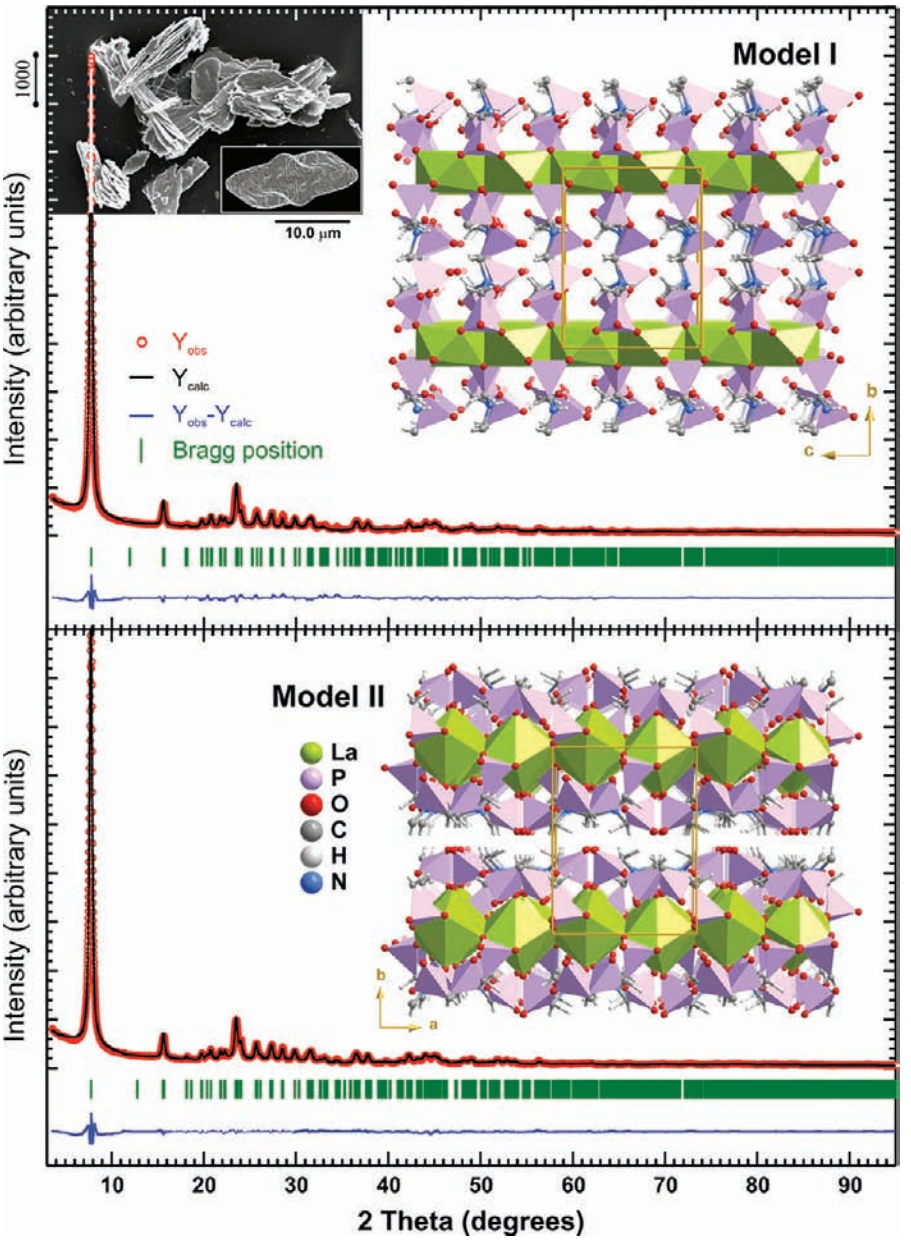

Figure 6. Final Rietveld plot (powder X-ray diffraction data) for the two models derived for the [La(L)] material (where L^{3-} = $[-(PO_3CH_2)_2-(NH)(CH_2PO_2)O_{1/2}-]_n^{3n-}$). Observed data points are indicated as red circles, and the best-fit profile (upper trace) and the difference pattern (lower trace) are drawn as solid black and blue lines, respectively. Green vertical bars indicate the angular positions of the allowed Bragg reflections. Refinement details are given in Table 1. Inset: SEM picture of the bulk material and a pictorial representation of the average crystallite shape as calculated from the Rietveld refinement (image created using GFourier[29] from the FullProf.2k[37] software suite).

treatment) is provided as Supporting Information (Figure S10). Ligand condensation above 300 °C leads to the release of water molecules with this process being clearly observed in the FT-IR spectra with a relative increase of the broad band centered at about 3400 cm^{-1} (see Figure S10, Supporting Information). Thermodiffractometry further shows that at 400 °C the thermal decomposition of **2** is almost complete. Concomitantly, the FT-IR spectrum is typical of an amorphous compound as also evidenced by the corresponding powder X-ray diffraction pattern (Figure S10, top in the Supporting Information).

The typical symmetric and asymmetric υ(C−H) and υ(N−H) stretching vibrational modes appear in the 3100−2800 cm^{-1} region. The latter mode is found at ca. 3037 cm^{-1}, unequivocally attributed to its displacement to ca. 2251 cm^{-1} upon deuteration (data not shown). Conversely, the large broad bands peaking at ca. 2950, 2925, 2873, and 2855 cm^{-1} (two sets) are, thus, assigned to $\upsilon_{sym+asym}$(C−H). In the 1500−1300 cm^{-1} region, a number of very weak bands are observed and can be assigned to υ(C−H) modes typical of P−CH_2 groups. The PO−H stretching modes were observed at ca. 2746 and 2615 cm^{-1} as very faint and broad bands that also completely disappear upon deuteration.

In the aforementioned 1500−700 cm^{-1} spectral region, the two central and very intense bands (found at ca. 1113 and 1074 cm^{-1}) are attributed to the υ(C−N) stretching vibrational modes typical of tertiary amines. Upon calcination these bands shift slightly to ca. 1103 and 1079 cm^{-1}, respectively, thus

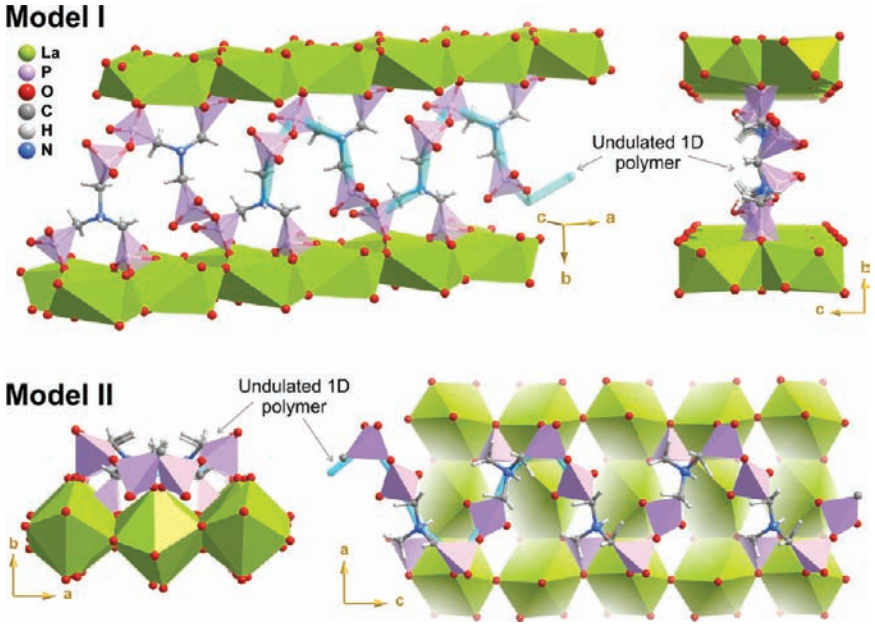

Figure 7. Perspective views of selective portions of the two structural models of **2** emphasizing the undulated 1D polymeric anionic ligand $[-(PO_3CH_2)_2(NH)(CH_2PO_2)O_{1/2}-]_n^{3n-}$. In model I, the polymer runs parallel to the [100] direction of the unit cell, pillaring adjacent lanthanum oxide layers. In model II the polymer is instead placed on top of the lanthanum oxide layers.

Table 3. Selected Bond Lengths (in Å) and Angles (In Degrees) for the La^{3+} Coordination Environment in Model I of [La(L)] (2) (Where L^{3-} = $[-(PO_3CH_2)_2(NH)(CH_2PO_2)O_{1/2}-]_n^{3n-}$)[a]

La(1)−O(1)	2.712(9)	La(1)−O(3)^{i}	2.683(9)
La(1)−O(1)^{i}	2.823(9)	La(1)−O(3)^{iii}	2.671(9)
La(1)−O(2)^{ii}	2.708(9)	La(1)−O(7)	2.647(9)
La(1)−O(2)^{iii}	2.799(9)	La(1)−O(7)^{ii}	2.714(9)
O1−La1−O1^{i}	140.5(4)	O2^{ii} −La1−O3^{i}	105.4(3)
O1−La1−O2^{ii}	143.4(4)	O2^{ii} −La1−O3^{iii}	95.6(3)
O1−La1−O2^{iii}	55.5(3)	O2^{iii} −La1−O3^{i}	100.7(4)
O1^{i} −La1−O2^{ii}	55.3(3)	O2^{iii} −La1−O3^{iii}	52.5(3)
O1^{i} −La1−O2^{iii}	136.8(4)	O2^{ii} −La1−O7	76.6(5)
O1−La1−O3^{i}	92.5(3)	O2^{ii} −La1−O7^{ii}	86.1(3)
O1−La1−O3^{iii}	106.4(3)	O2^{iii} −La1−O7	137.0(4)
O1^{i} −La1−O3^{i}	51.7(3)	O2^{iii} −La1−O7^{ii}	67.3(4)
O1^{i} −La1−O3^{iii}	103.5(4)	O3^{i} −La1−O3^{iii}	113.3(4)
O1−La1−O7	84.8(4)	O3^{i} −La1−O7	61.6(3)
O1−La1−O7^{ii}	79.9(3)	O3^{i}−La1−O7^{ii}	168.0(4)
O1^{i} −La1−O7	64.9(3)	O3^{iii} −La1−O7	168.3(4)
O1^{i}−La1−O7^{ii}	138.1(4)	O3^{iii} −La1−O7^{ii}	60.9(3)
O2^{ii} −La1−O2^{iii}	145.3(3)	O7^{ii} −La1−O7	126.1(3)

[a] Symmetry transformations used to generate equivalent atoms: (i) −1/2 + *x*, −*y*, *z*; (ii) 1/2 − *x*, *y*, −1/2 + *z*; (iii) 1 − *x*, −*y*, −1/2 + *z*.

Table 4. Selected Bond Lengths (in Å) and Angles (In Degrees) for the La^{3+} Coordination Environment in Model II of [La(L)] (2) (Where L^{3-} = $[-(PO_3CH_2)_2(NH)(CH_2PO_2)O_{1/2}-]_n^{3n-}$)[a]

La1−O1	2.595(10)	La1−O3^{ii}	2.605(10)
La1−O1^{i}	2.576(10)	La1−O3^{iii}	2.543(10)
La1−O2	2.621(10)	La1−O6	2.657(9)
La1−O2^{ii}	2.634(10)	La1−O8^{iii}	2.586(10)
O1−La1−O2	56.9(4)	O2−La1−O3^{ii}	118.9(5)
O1−La1−O6	71.3(5)	O2−La1−O3^{iii}	120.1(6)
O1−La1−O2^{ii}	111.3(5)	O2−La1−O8^{iii}	131.4(6)
O1−La1−O3^{ii}	158.6(6)	O2^{ii} −La1−O2	137.5(5)
O1−La1−O3^{iii}	63.4(4)	O2^{ii} −La1−O6	66.0(5)
O1−La1−O8^{iii}	118.6(6)	O2^{ii} −La1−O3^{ii}	55.7(4)
O1^{i} −La1−O1	128.5(6)	O2^{ii} −La1−O3^{iii}	69.3(4)
O1^{i} −La1−O2	76.9(5)	O2^{ii} −La1−O8^{iii}	90.9(5)
O1^{i} −La1−O6	117.2(6)	O3^{ii} −La1−O6	87.4(5)
O1^{i} −La1−O2^{ii}	118.3(6)	O3^{ii} −La1−O3^{iii}	118.3(5)
O1^{i} −La1−O3^{ii}	62.8(4)	O3^{ii} −La1−O8^{iii}	80.6(5)
O1^{i} −La1−O3^{iii}	148.0(6)	O3^{iii} −La1−O6	94.5(6)
O1^{i} −La1−O8^{iii}	74.5(5)	O3^{iii} −La1−O8^{iii}	74.3(5)
O2−La1−O6	71.8(5)	O6−La1−O8^{iii}	156.8(6)

[a] Symmetry transformations used to generate equivalent atoms: (i) 1/2 + *x*, −*y*, *z*; (ii) 1.5 − *x*, *y*, 1/2 + *z*; (iii) 1 − *x*, −*y*, 1/2 + *z*.

pointing to a small structural modification for this section of the molecule. The υ(P−C) stretching vibrational modes, found in the ca. 790−680 cm^{-1} region, are also markedly present in both spectra. Remarkably, and as clearly depicted in Figure 9, these bands which are directly associated with the central portion of the ligand become significantly narrower upon phase transition. This feature indicates the formation of a more rigid, constrained structure, coherent with the proposed 2D-to-3D or 2D-to-2D transition and with the results derived from the photoluminescence studies.

A number of modifications are also notably visible in the regions attributed to the υ(P═O) (from ca. 1250 to 1150 cm^{-1}) and υ(P−O) (from ca. 1050 to 900 cm^{-1}) stretching vibrational modes (Figure 9). It is worth noting the simultaneous appearance of a new band centered at about 929 cm^{-1} and the increase of the number of bands in the 1250−1150 cm^{-1}

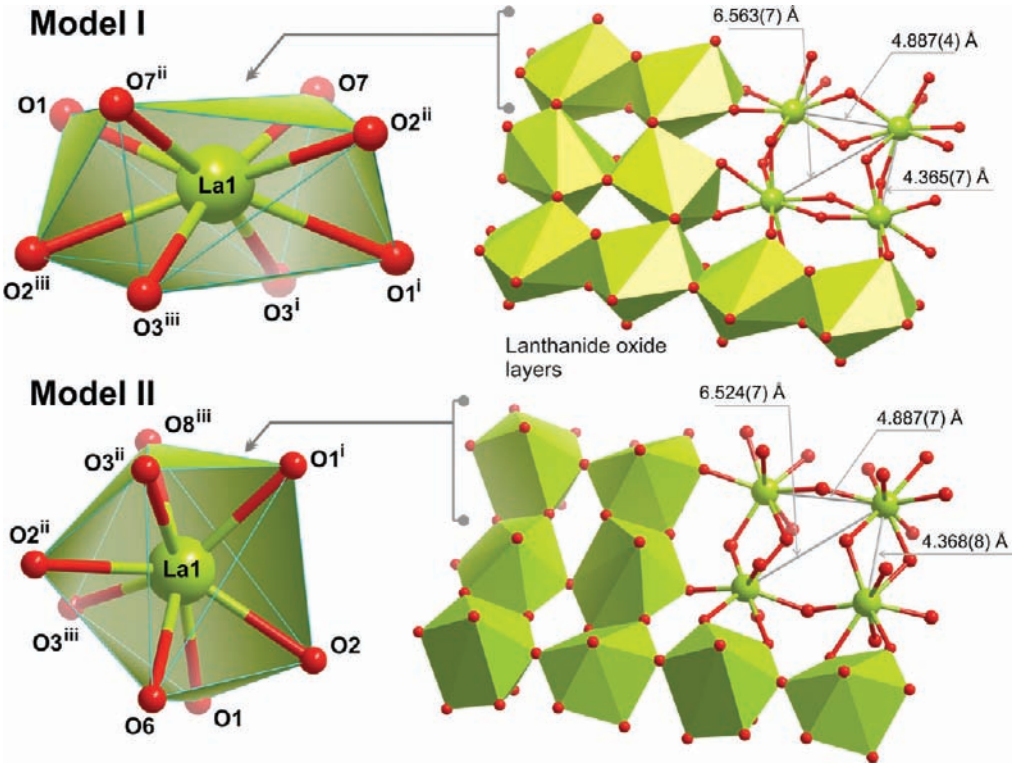

Figure 8. Highly distorted $\{LaO_8\}$ square antiprismatic (model I) and bicapped trigonal prismatic (model II) coordination environments modeled for La^{3+} in compound **2**. For selected bond lengths (in Å) and angles (in degrees) see Tables 3 and 4. On the side there are also depicted portions of the compact two-dimensional lanthanum oxide layers for the two models of **2**, depicting the edge-sharing connectivity between adjacent $\{LaO_8\}$ polyhedra. Symmetry transformations are used to generate equivalent atoms. Model I: (i) $-1/2 + x, -y, z$; (ii) $1/2 - x, y, -1/2 + z$; (iii) $1 - x, -y, -1/2 + z$. Model II: (i) $1/2 + x, -y, z$; (ii) $1.5 - x, y, 1/2 + z$; (iii) $1 - x, -y, -1/2 + z$.

region. These modifications are in line with the formation of pyrophosphonates.[26]

2.6. Look Into the Structural Transformation of [La(H$_3$nmp)] into [La(L)]. The transformation of layered $[La(H_3nmp)]$ (**1**) into either the 3D or 2D networks $[La(L)]$ (**2**) (where $L^{3-} = [-(PO_3CH_2)_2(NH)(CH_2PO_2)O_{1/2}-]_n^{3n-}$) occurs in a microcrystal-to-microcrystal type fashion. In both models the lanthanum oxide layers remain approximately in the same location, and the transformation occurs mainly in the interlayer space involving individual blocks of the organic ligand. The connectivity of the P1 phosphonate group (Figures S11b and S11d in the Supporting Information) does not change significantly during this transformation: the group remains strongly chelated to four adjacent La^{3+} centers via six La−O bonds. Therefore, structural modification must be solely driven by the inherent structural freedom associated with the individual P2 and P3 moieties which decorate the surfaces of the lanthanum oxide layer.

From the crystal structure of **1**, one can observe that the diprotonated $-CH_2PO_3H_2$ moiety is the most weakly bonded to the layer: (i) on one hand, this tetrahedral group is only bound to a single La^{3+} cation; (ii) on the other, this single La−O bond is the longest (and, thus, the weakest) among all belonging to the phosphonate groups which protrude into the interlayer space [La1−O4 of 2.634(8) Å]. It is, thus, feasible to assume that the externally driven increase in temperature can easily promote the rupture of this bond. Indeed, independently of the model assumed, the formation of the polymeric L^{3-} ligand starts always with modifications in the connectivity of this diprotonated $-CH_2PO_3H_2$ moiety, which becomes free and able to react with neighboring moieties.

Model I. In one approach, the $-CH_2PO_3H_2$ group may migrate to the interlayer space and approach the lanthanum oxide layer immediately above. Because of bond constraints, this process must necessarily be accompanied by a rotation of the entire organic molecule (as depicted in Figure S11 in the Supporting Information), ultimately promoting a modification of the coordination fashion of the P3 phosphonate group (step 3 in Figure S11b in the Supporting Information): one oxygen atom establishes a new μ_2 bridge between adjacent La^{3+} cations, with the newly formed free oxygen being available to react with the migrating $-CH_2PO_3H_2$ group from the adjacent layer. We note that this type of rotation associated with phosphonate groups within crystalline hybrid frameworks, promoting distinct coordination fashions, has already been reported in the past using single-crystal X-ray diffraction studies.[27] The condensation reaction between groups leads to the release of one water molecule (as observed from the TGA measurements) and the concomitant formation of the one-dimensional organic ligand based on a pyrophosphonate connection. A pictorial representation of this transformation in the form of a storyboard-like cartoon (Figure S12) and a movie of the transformation are provided as Supporting Information.

Model II. The second model is less straightforward to derive as it requires an inversion of the *a*- and *c*-axes of the parent unit cell of compound **1**. This change in unit cell parameters ultimately allows a smaller migration of the $-CH_2PO_3H_2$ group, which only rotates on top of the lanthanum oxide layer approaching the P3

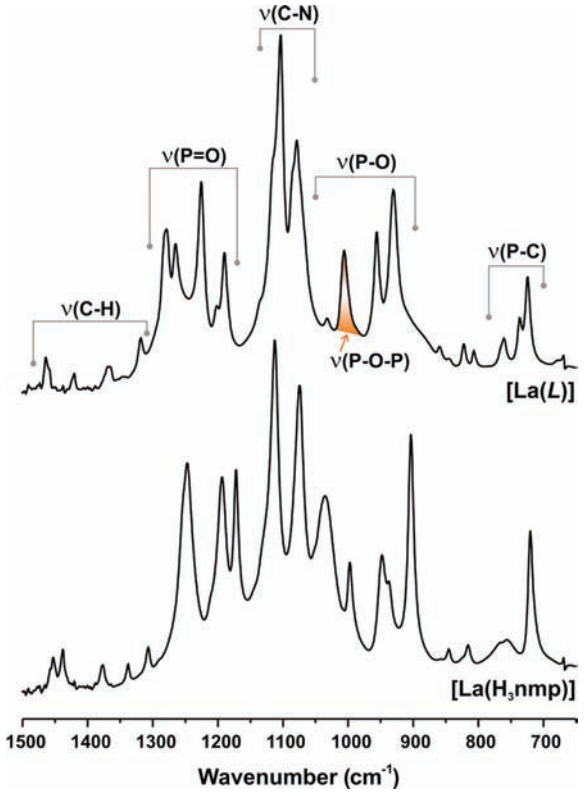

Figure 9. Comparison between the FT-IR spectral features of [La(H_3nmp)] (**1**) with [La(L)] (**2**) in the 1500−650 cm^{-1} region.

phosphonate group of an adjacent organic moiety (located on the same side of the inorganic layer, see Figure S13 in the Supporting Information). As in the previous model, the approaching groups condensate, leading to the release of one water molecule. The pictorial representation of this alternative transformation is given in Figure S14 (in the Supporting Information), and the corresponding movie is also provided as an electronic MOV file. Noteworthy, despite this smaller structural modification, the modeled crystal structure could only be obtained using the same battery of constraints as for model I, even though the reliability factors summarized in Table 1 are slightly better.

This crystalline structural transformation has a strong impact on the unit cell metrics of **2**, even though the overall symmetry remains intact (both materials crystallize in the $Pca2_1$ space group; see Table 1). Surprisingly, using as example model I (which does not require the inversion of the unit cell axes), along the *b*-axis (which corresponds to the interlayer distance, see Figures 3 and 6) the unit cell only shrinks by ca. 3.3%. It is across the lanthanum oxide layers, in particular parallel to the *c*-axis (see Figure 4a), that the La^{3+} metallic centers become significantly closer, going from 4.819(2) to 4.365(7) Å (corresponding to a shrinkage of about 11.2% of the cell axis). This occurs because the local rearrangement of the lanthanum oxide layers described above promotes a coalescence of the La^{3+} polyhedra, which are corner-shared in **1** (Figure 4a) and become edge-shared in **2** due to a newly formed μ_2-bridge (Figure S11d in the Supporting Information).

The research group of Clearfield has reported supramolecular arrays in which $H_{6-x}nmp^{x-}$ residues self-assemble in the solid state with heterocyclic amines,[28] leading to the formation of honeycomb-type or one-dimensional chains. Noteworthy, these organic crystals exhibit a distribution of $H_{6-x}nmp^{x-}$ residues resembling that of

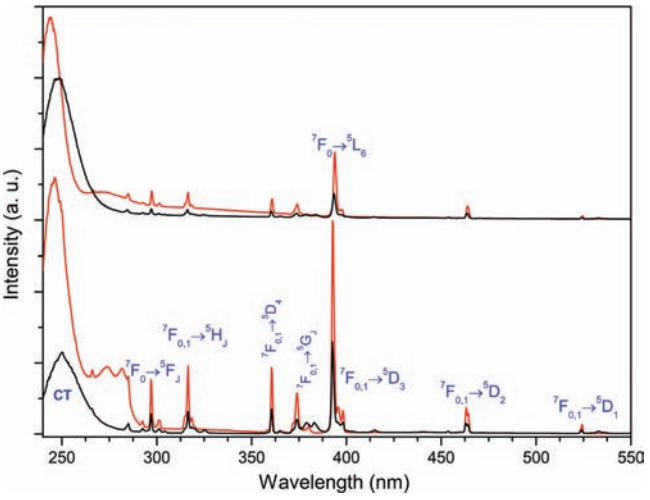

Figure 10. Excitation spectra of (bottom) [($La_{0.95}Eu_{0.05}$)(H_3nmp)] and (top) [($La_{0.95}Eu_{0.05}$)(L)] recorded at ambient temperature (black line) and at 11 K (red line), while monitoring the emission at 618 nm. The intensity is only comparable for the variation of the temperature for each sample, not between different samples.

the $[-(PO_3CH_2)_2(NH)(CH_2PO_2)O_{1/2}-]_n^{3n-}$ ligand in **2**. The scaffold of these arrays is essentially maintained by strong and highly directional P−O^-···HO−P hydrogen bonding interactions, which may be envisioned as the supramolecular precursors of potential pyrophosphonate bonds (P−O−P). The thermogravimetric studies of the compound with protonated 1,7-phenanthroline reported by Sharma and Clearfield[28] reveal a total loss of about four water molecules (in two stages) per formula unit up to 260 °C. Because their structure only contains two water molecules of crystallization, we now (while comparing with our material) infer that the remaining loss most certainly arises from the formation of pyrophosphonates from the P−O^-···HO−P interactions: during the first loss (up to 150 °C) crystallinity is maintained; heating up the compound (between 150 and 260 °C) the following weight loss leads to a completely amorphous compound which could not be characterized. Because **2** is still a crystalline material and the transformation occurs at a higher temperature (above ca. 300 °C), we infer that the lanthanum oxide layers which confine the H_3nmp^{3-} residues act as insulating coordinating inorganic blocks templating, on the one hand, the condensation reaction and, on the other, retaining some degree of structural crystallinity.

To be able to isolate crystalline **2** with a higher degree of crystallinity, the structural transformations rationalized in the previous paragraphs must necessarily occur in a single step to avoid overall connection mistakes. This does not seem to be the case as the isolated material is poorly crystalline. The pattern is dominated by the (010) reflection arising from the lanthanum oxide layer (Figure 7), with the very weak and broad reflections observed above ca. 25° 2θ being indicative of a poorly organized interlayer structure filled with defects. Because the overall crystallite morphology is not significantly modified, we then infer that calcination leads instead to the formation of nanosized domains within the crystallites. This assumption is supported by two facts. First, microstructural analysis performed using powder X-ray diffraction indicates, for either of the proposed structural models, an average crystallite size of ca. 255 nm (with standard deviation of 85 nm). The shape of this average crystallite (as produced by

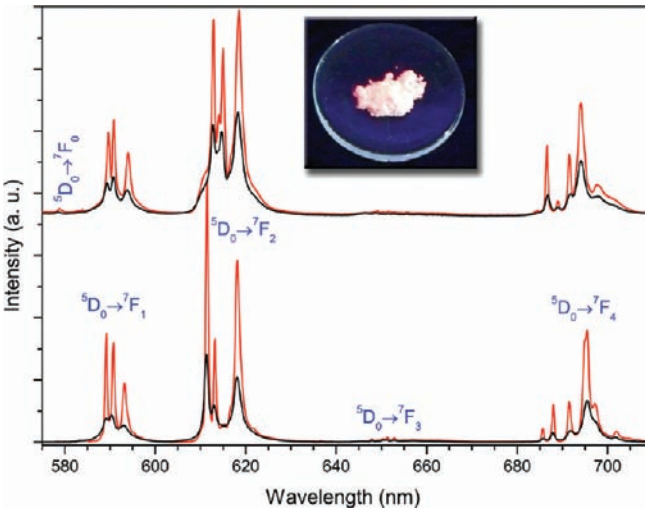

Figure 11. Emission spectra of (bottom) $[(La_{0.95}Eu_{0.05})(H_3nmp)]$ and (top) $[(La_{0.95}Eu_{0.05})(L)$, with excitation at 393 and 394 nm, respectively, recorded at ambient temperature (black line) and at 11 K (red line). The intensity is only comparable for the variation of the temperature for each sample, not between different samples. The inset depicts the characteristic red emission of Eu^{3+} when $[(La_{0.95}Eu_{0.05})(H_3nmp)]$ is irradiated with a laboratory UV lamp (wavelength of 254 nm).

GFourier[29]) is depicted in Figure 6 as an inset next to the SEM picture. Second, TEM images of the calcined material **2** clearly show a modification of the crystallites, which evidence the presence of (nanosized) domains with different contrast and holes in the crystal (see Figure S22 in the Supporting Information).

2.7. Photoluminescent Properties. As described in section 2.1.4, the doped $[(La_{0.95}Eu_{0.05})(H_3nmp)]$ (**1**−**LaEu**) and $[(La_{0.95}Tb_{0.05})(H_3nmp)]$ (**1**−**LaTb**) compounds could be readily prepared, and the materials emit the characteristic red (inset in Figure 11) and green (inset in Figure S16 in the Supporting Information) colors when irradiated under UV light. The photoluminescent properties detailed below will be focused in the **1**−**LaEu** material and the dense 3D/2D network obtained by its calcination, $[(La_{0.95}Eu_{0.05})(L)]$ (**2**−**LaEu**). The excitation and emission spectra of **1**−**LaTb** are provided in the Supporting Information (see Figures S15 and S16, respectively).

The excitation spectra of **1**−**LaEu** and **2**−**LaEu**, recorded at ambient temperature and 11 K (Figure 10), display a series of sharp lines typical of the Eu^{3+} intra-$4f^6$ transitions, namely: $^7F_{0,1} \rightarrow {}^5D_{4-0}$, $^5L_6$, $^5G_{2-6}$, $^5H_{3-7}$, and $^5F_{1-5}$. On the high-energy region, the spectra exhibit at 11 K an additional and well-defined broad band attributed to ligand-to-Eu^{3+} charge transfer (CT), peaking at 246.0 and 243.9 nm for **1**−**LaEu** and **2**−**LaEu**, respectively. The corresponding energies (5.04 and 5.08 eV) and fwhm (0.24 and 0.23 eV) of the CT bands are in the range of the values reported for related compounds containing Eu^{3+}.[30] As discussed in the following paragraphs, the extra broad peaks at 274 and 282 nm of **1**−**LaEu** and the broad UV band from ca. 270 to 350 nm of **2**−**LaEu** are mostly due to the presence of a very small amount of an unidentified impurity phase which also contains Eu^{3+}.

Figure 11 shows the emission spectra of **1**−**LaEu** and **2**−**LaEu** excited at 393 and 394 nm, respectively. The sharp lines are assigned to transitions between the first excited non-degenerate $^5D_0$ state and the $^7F_{0-4}$ levels of the fundamental Eu^{3+} septet. Except for the $^5D_0 \rightarrow {}^7F_1$ lines, which have a predominant magnetic-dipole character independent of the Eu^{3+} crystallographic site, the observed transitions are mainly of electric-dipole nature. The local-field splitting of the $^7F_{1,2}$ levels into three and a maximum of five Stark components, respectively, and the predominance of the $^5D_0 \rightarrow {}^7F_2$ transition in relation to the $^5D_0 \rightarrow {}^7F_1$ one indicate the presence of a single low-symmetry Eu^{3+} environment for both **1**−**LaEu** and **2**−**LaEu**. This result is in good agreement with the crystallographic evidence described above. As mentioned above, **1**−**LaEu** and **2**−**LaEu** exhibit a number of structural similarities such as the local Eu^{3+} symmetry and multiplicity. However, their emission properties allow us to infer some important distinctions between the two compounds: (i) **1**−**LaEu** has sharper emission lines, particularly at 11 K, characteristic of a compound with higher crystallinity; (ii) the integrated intensity ratios between ambient temperature and 11 K (II_{RT}/II_{11K}), 1.79 and 1.34 for **1**−**LaEu** and **2**−**LaEu**, respectively, indicate a more flexible structure (a more temperature-dependent photoluminescence) for the former material; (iii) the integrated intensity ratio $R = {}^5D_0 \rightarrow {}^7F_2/{}^5D_0 \rightarrow {}^7F_1$, also known as asymmetry ratio and calculated as 2.50 and 3.25 for **1**−**LaEu** and **2**−**LaEu**, respectively, indicates a higher asymmetry of the Eu^{3+} coordination polyhedron for the latter material (please note: the lower the *R*-value, the higher the site symmetry of the Eu^{3+}), in good agreement with the X-ray diffraction studies.

Although the emission spectra of the two compounds can be attributed to the presence of a single Eu^{3+} site with low symmetry, a detailed analysis allows the detection of additional Eu^{3+} signals, which, on the present situation, are attributed to a very small amount of an impurity phase. For example, Figure S17 in the Supporting Information shows a magnification of the region of the nondegenerated $^5D_0 \rightarrow {}^7F_0$ transition, and Figure S18 (also in the Supporting Information) compares, at 11 K, the

Scheme 2. Reaction of Styrene Oxide with an Alcohol (Methanol or Ethanol) in the Presence of the Catalyst $[La(H_3nmp)]$ to Give the Respective 2-Alkoxyalcohol Products

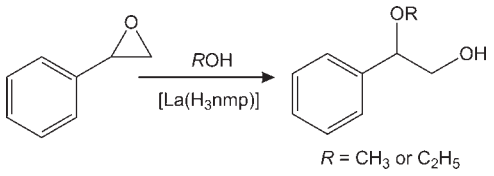

Table 5. Ring Opening of Styrene Oxide with Methanol[a]

catalyst	temperature (°C)	time (h)	conversion[b] (%)	selectivity[c] (%)
none	40	72	8	100
H_6nmp	40	1	100	100
$LaCl_3 \cdot 7H_2O$	40	24	71	93[d]
1	40	24/48/72	40/77/100	100/100/100
1	55	24/48	76/100[b]	100/100

[a] Reaction conditions: PhEtO (0.83 mmol), catalyst (34.7 mg, 0.08 mmol of La^{3+}), alcohol (2 mL). [b] Conversion of PhEtO. [c] Selectivity to MeOPhEtOH. [d] A chlorophenylethyl alcohol product and 2-methoxyphenyl ethanol were formed in ca. 6% and 1% selectivity.

dx.doi.org/10.1021/ja205243w |*J. Am. Chem. Soc.* 2011, 133, 15120–15138

former emission spectra with those collected when exciting on the selected unattributed UV bands. These inorganic impurities, also detected by solid-state NMR (Figure S8 in the Supporting Information), electron microscopy, and powder X-ray diffraction studies (Figure S21 in the Supporting Information), become slightly more evident in the photoluminescence studies at either low temperature with selected excitation or ambient temperature with the very sensitive $^5D_0 \rightarrow {}^7F_0$ transition. We must stress that attempts to remove or, at least, diminish the amount of these impurities proved to be unsuccessful. In addition, due to their presence in a very small amount, their identification was not possible (only two reflections were observed in the powder X-ray diffraction pattern).

The $^5D_0$ lifetimes of Eu^{3+} of **1**−**LaEu** and **2**−**LaEu** were determined by monitoring the emission decay curves within the $^5D_0 \rightarrow {}^7F_2$ transition (618 nm) at ambient temperature and 11 K, using an excitation at ca. 394 nm (Figures S19 and S20 in the Supporting Information). The decay curves were well-fitted by single exponential functions, yielding lifetimes for **1**−**LaEu** of 2.09 ± 0.01 and 2.31 ± 0.01 ms, at ambient temperature and 11 K, and 2.04 ± 0.01 and 2.08 ± 0.01 ms, at ambient temperature and 11 K, respectively, for **2**−**LaEu**. Changing the monitoring and/or excitation wavelength can result in the detection of more complex exponential curves (not shown) due to the detection of the aforementioned secondary inorganic phases. As discussed above, **2**−**LaEu** shows a smaller dependence of the Eu^{3+} lifetime with the temperature, which is a typical behavior of a rigid structure.[31] Furthermore, the shorter lifetime values for this material can only be justified by its lower crystallinity and possible presence of local defects. These two conclusions agree well with the assumptions highlighted above in the description of the crystal structures.

2.8. Heterogeneous Catalysis. The [La(H_3nmp)] (**1**) material revealed itself to be a promising catalyst in the ring-opening reaction of styrene oxide (PhEtO) with methanol or ethanol (Scheme 2). The reaction of PhEtO with methanol in the presence of **1** at 40 °C gives 2-methoxy-2-phenylethanol (MeOPhEtOH) in quantitative yields within 72 h reaction (Table 5); in the absence of a catalyst the reaction under similar conditions was very sluggish, and only 8% conversion was reached in the same period of time. These results indicate excellent regioselectivity to the β-alkoxy alcohol, which may be formed by nucleophilic attack of the alcohol at the phenyl-substituted carbon atom.[32] The reaction of 2-phenylethanol with methanol in the presence of **1** does not take place, suggesting that the mechanism does not involve the condensation of a β-hydroxyl intermediate with the alcohol. According to the literature, the MOF catalyst may thus coordinate with PhEtO by way of an acid−base interaction to produce an increase in the electrophilic nature (partial positive charge) of the more substituted carbon of the substrate (polarization of the C−O bond), which in turn is attacked by the alcohol to yield the β-alkoxy alcohol product.[32a] Despite the catalytic activity of **1** being lower than that reported for the Fe- or Cu-MOFs used as catalysts in the same reaction at 40 °C (more than 92% conversion at 1 h reaction),[33] the selectivity to MeOPhEtOH is always 100%. Indeed, for the transition metal MOFs, selectivity toward the same product at more than 92% conversion reached, at best, ca. 95%.[33] Similar excellent regioselectivities to the β-alkoxy alcohol product have also been reported for lanthanide-containing heterodimetallic coordination polymers in the alcoholysis ring-opening reaction of PhEtO.[32b]

When a mixture of water/acetonitrile (1:3) is used instead of methanol (total volume of the reaction mixture was the same as for the catalytic alcoholysis reactions), no ring opening of PhEtO in the presence of **1** is observed (40 °C, 72 h). These results contrast with that reported in the literature for decatungstocerate(IV) used as catalyst (0.04 M) in the same reaction, which also exhibited activity in the hydrolysis of the epoxide to the corresponding diol.[34] Therefore, **1** possesses alcoholysis but no hydrolysis activity.

Table 6. Ring Opening of Styrene Oxide with Ethanol[a]

catalyst	temperature (°C)	time (h)	conversion[b] (%)	selectivity[c] (%)
none	55	72	4	100
1	55	24/48/72	23/60/100	100/100/100
1	70	24/48	77/100[b]	100/100

[a] Reaction conditions: PhEtO (0.83 mmol), catalyst (34.7 mg, 0.08 mmol of La^{3+}), alcohol (2 mL). [b] Conversion of PhEtO. [c] Selectivity to EtOPhEtOH.

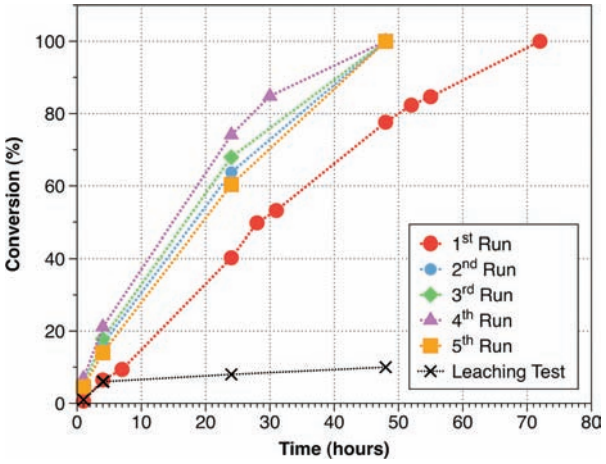

Figure 12. Recycling tests on the use of [La(H_3nmp)] (**1**) as a heterogeneous catalyst in the ring-opening reaction of styrene oxide with methanol at 40 °C. Experimental data points are connected by a dotted line for indicative purposes only.

For comparative purposes, the reactants H_6nmp and $LaCl_3 \cdot 7H_2O$ were also tested as catalysts in the methanolysis of PhEtO, at 40 °C, using molar ratios of (H_6nmp or La^{3+})/PhEtO/methanol equivalent to those for **1** (Table 5). When $LaCl_3 \cdot 7H_2O$ was employed as the (Lewis acid) catalyst, MeOPhEtOH is formed in 93% selectivity at 71% conversion, reached at 24 h reaction; a chlorophenylethyl alcohol product and 2-methoxyphenyl ethanol were formed with ca. 6% and 1% selectivity, respectively. High catalytic activity and regioselectivity to the β-alkoxy alcohol product has been reported by Berkessel et al.[35] for rare-earth triflates used as homogeneous catalysts in the alcoholysis of PhEtO under mild reaction conditions. A catalytic amount of H_6nmp gives MeOPhEtOH in quantitative yields after only 1 h of reaction. These results indicate that the synthetic precursors are more active than **1** itself, possibly due to the low amount of accessible active sites in the latter case. It is worth mentioning that the synthetic precursor H_6nmp dissolves completely in the reaction medium and is, thus, a homogeneous catalyst which requires significantly more demanding separation and purification processes than for the heterogeneous catalyst **1**. On the other hand, the synthetic precursor $LaCl_3 \cdot 7H_2O$ dissolves completely in the initial stage of the reaction, and eventually a

suspension is formed. The homo/heterogeneous nature of the catalytic reaction for the case of $LaCl_3 \cdot 7H_2O$ was investigated by performing a separate experiment which consisted of filtering the solid (white in color) through a 0.20 μm nylon GVS membrane, after 4 h reaction, at 40 °C, and leaving the reaction solution under agitation a further 20 h. The increment in conversion in the interval of time 4−24 h was 38% which is similar to that observed for the experiment without filtration (41%). Hence, although the reaction of PhEtO is much faster for $LaCl_3 \cdot 7H_2O$ than for **1**, in the former case the catalytic reaction is less selective and homogeneous in nature.

The rate of conversion of PhEtO into MeOPhEtOH (in quantitative yields without affecting product selectivity) in the presence of **1** could be increased by increasing the reaction temperature from 40 to 55 °C (Table 5).

The catalytic performance of **1** was further investigated in the reaction of PhEtO with ethanol. The sole product was 2-ethoxy-2-phenylethanol (EtOPhEtOH), which was obtained in quantitative yields within 72 h of reaction (Table 6). We note that without the catalyst the PhEtO conversion was negligible. A temperature increase from 55 to 70 °C enhances considerably the rate of ethanolysis of PhEtO. The reaction of PhEtO is slower in ethanol than in methanol (Tables 5 and 6), which may be attributed to the inherent steric hindrance of each alcohol. No secondary reactions of ethanol were detected, indicating an excellent productive consumption of the alcohol in the ring-opening reaction. To check if the ring opening of PhEtO via hydrolysis can be a competitive reaction, a separate catalytic test was performed using PhEtO/H_2O/ethanol molar ratios of 1:2:19, at 70 °C. The presence of excess water relative to the substrate did not influence the product selectivity (EtOPhEtOH was always the only reaction product), but catalytic activity decreased; conversion at 24 h was 42% compared to 77% without adding water (Table 6). As discussed above, in section 2.4, water may bind to defect sites of **1** which may be responsible for the catalytic reaction. Accordingly, excess water may inhibit the catalytic activity of **1**, explaining the decrease in reaction rate observed when water was added to the reaction mixture.

The recyclability of catalyst **1** was investigated in five consecutive batch runs of the reaction of PhEtO with methanol at 40 °C. Prior to reuse, the solid catalyst was separated by centrifugation, washed with *n*-hexane, and dried at ambient temperature overnight. In all runs, MeOPhEtOH was always the sole product. An increase in the reaction rate was clearly observed from the first to the second run; the catalytic activity remained roughly constant in subsequent runs (Figure 12). The structural integrity of the regenerated catalyst was inspected using *in tandem* powder X-ray diffraction, vibrational spectroscopy, and electron microscopy studies (Figure S23 in the Supporting Information). No significant modifications were detected in the structure of the material even though a small reduction of the overall crystallinity was observed. After the catalytic process, the bulk catalyst was isolated as very small particles characterized by an undefined morphology, which most certainly results from the cracking of the starting crystallites of **1**. This crystal fragmentation explains, on the one hand, the observed reduction in crystallinity and, on the other, the positive effect on the catalytic performance in subsequent catalytic runs by way of an increase of the number of accessible active sites which may be defects.

To get a better insight into the hetero/homogeneous nature of the catalytic reaction, a leaching test was performed for **1** by filtering the used catalysts through a 0.20 μm nylon GVS membrane (after 4 h reaction, at 40 °C) and leaving the reaction solution under stirring for a further 20 h. The increment in conversion in the period of time 4−24 h was negligible, indicating **1** is a truly heterogeneous catalyst (Figure 12).

The [La(L)] (**2**) material was tested as a catalyst in the reaction of PhEtO with methanol at 55 °C, under conditions similar to those used for **1**. The only reaction product was MeOPhEtOH obtained in quantitative yield within 4 h, indicating that **2** is much more active than **1**. The crystalline structure of **2** was preserved during the catalytic reaction (ascertained by powder X-ray diffraction). We note that the catalytic activity of **2** is somewhat comparable and product selectivity superior to that reported in the literature for transition metal−organic frameworks.[32] As discussed above, **2** is a less crystalline material than **1** and therefore may possess a greater amount of local defect sites, which could explain the considerably faster reaction of PhEtO in the case of **2**. Indeed, TEM images of **2** clearly depict a significant increase of widespread structural defects of the individual crystallites (see Figure S22 in the Supporting Information).

3. CONCLUDING REMARKS

In the present study, we have shown that by using different synthetic conditions, based on microwave heating or a dynamic hydrothermal synthesis (i.e., with the reaction vessels spinning at a constant rate during the entire period of reaction), the lanthanide/nitrilotris(methylenephosphonic acid) system can lead to the preparation of a whole new layered material: [La(H_3nmp)] (**1**). Independently of the employed synthetic method, it was found that this compound could only be isolated when the lanthanide oxide layer is based on La^{3+}; other lanthanide centers promote the formation of mixtures of which ([La(H_3nmp)]$\cdot 1.5H_2O$) is, in most of the cases, one of the main constituents. Photoluminescent materials could be, however, successfully engineered by the selective inclusion of stoichiometric amounts (5%) of optically active Eu^{3+} and Tb^{3+} centers in the reactive mixtures.

In opposition to that reported for [La(H_3nmp)]$\cdot 1.5H_2O$, **1** does not have any solvent molecules incorporated into the network, and, upon heating, the structure is transformed into a dense novel 3D or a layered 2D material formulated as [La(L)] (**2**) (where $L^{3-} = [-(PO_3CH_2)_2(NH)(CH_2PO_2)O_{1/2}-]_n^{3n-}$). Because the two compounds could only be prepared as microcrystalline powders, structural solution was not trivial and had to be ultimately based on powder X-ray diffraction studies (in conjunction with data from FT-IR spectroscopy, ^{13}C and ^{31}P solid-state NMR, and themogravimetry). We have further shown (using X-ray powder data) that the thermal transformation of **1** into **2** was accompanied by the creation of nanosized domains within the crystallites.

The present work shows that small structural changes in the overall connectivity of the organic ligand can promote important differences in the overall thermal behavior and stability of the materials. In the previous material reported by us, heating-induced dehydration of the network (which was partially reversible when the temperature was decreased) was immediately followed by thermal decomposition. The layered compound herein reported suffers instead, between 300 and 400 °C, a structural transformation into a novel structure, which remains unaltered when the system is cooled to ambient temperature. This occurs because the H_3nmp^{3-} anionic ligand undergoes an

in situ polymerization (condensation) into a novel polymeric anionic ligand which was formulated as $[-(PO_3CH_2)_2(NH)(CH_2PO_2)O_{1/2}-]_n^{3n-}$. It was shown that this polymerization can occur either on top of the lanthanide oxide layers or across adjacent layers, promoting either 2D or 3D materials with the same crystal symmetry; due to the poor crystallinity of the final compound, powder X-ray diffraction could not unequivocally show which process occurs preferentially. To the best of our knowledge, this type of structural change, mostly focused in the organic ligand, is clearly unprecedented. Prior work from the research group of Clearfield on organic crystals further shows that the lanthanum oxide layers of **1** act as simultaneously insulating and templating scaffolds having, thus, a strong influence on the formation of this unprecedented one-dimensional polymeric ligand. The transformation process was further accompanied using FT-IR and solid-state NMR studies, and we have devised a schematic model representation based on the modeled structures to illustrate the dynamics and transformation of the system when the temperature is increased.

We demonstrated that lanthanide cations can be included and uniformly distributed among the La^{3+} matrix (as shown by electron microscopy studies), promoting the isolation of red- and green-emitting materials ($[(La_{0.95}Eu_{0.05})(H_3nmp)]$ and $[(La_{0.95}Tb_{0.05})(H_3nmp)]$, respectively) when irradiated upon UV light. The photoluminescent properties of layered $[(La_{0.95}Eu_{0.05})(H_3nmp)]$ and $[(La_{0.95}Eu_{0.05})(L)]$ materials have shown the presence of a single crystallographic lanthanide center with lifetimes ranging from 2.04 ± 0.01 to 2.31 ± 0.01 ms for both materials (at ambient and lower temperature). These studies were also particularly informative regarding the robustness of the isolated compounds: while the layered material yielded sharp emission lines and a higher II_{RT}/II_{11K} ratio of integrated intensities, which indicates the presence of a highly crystalline material with some structural flexibility, for the calcined structure the integrated intensity ratio, $R = {}^5D_0 \rightarrow {}^7F_2/{}^5D_0 \rightarrow {}^7F_1$, points to a highly distorted Eu^{3+} coordination environment.

$[La(H_3nmp)]$ is an effective heterogeneous catalyst in the ring-opening reaction of styrene oxide with methanol and ethanol producing, respectively, 2-methoxy-2-phenylethanol or 2-ethoxy-2-phenylethanol. Outstanding features of its catalytic performance may be pointed out as:

(i) excellent regioselectivity toward the β-alkoxy product, formed in quantitative yields, under quite mild reaction conditions (ca. atmospheric pressure, less than 70 °C, without cosolvents);
(ii) it possesses alcoholysis activity but no hydrolysis activity, and thus, competitive epoxide ring-opening reactions in the presence of water do not take place;
(iii) the reaction rate may be enhanced by increasing the reaction temperature, without affecting product selectivity;
(iv) it may be recycled without the need for regeneration treatments (only simple washing and drying at ambient temperature) and no drops in catalytic activity and product selectivity;
(v) the catalytic reaction is heterogeneous in nature.

It is postulated that the active sites are structural defect sites based on the following results: the reused catalyst is somewhat less crystalline and more active than the fresh catalyst; water which may coordinate to defect sites has an inhibitory role, decreasing the catalytic activity. On the other hand, the material $[La(L)]$ (formed by the thermal treatment of **1**) is a less crystalline material than **1**, while it exhibited similar excellent regioselectivity toward the β-alkoxy product and much higher catalytic activity than the parent compound.

Currently, we are investigating the possibility to isolate new materials using the same synthetic procedures herein employed (based on microwave heating or on dynamic hydrothermal synthesis) but containing distinct lanthanide centers. The main goal is also clearly focused on the reduction of crystallite size. From the current study, we envisage that nanosized crystallites of these materials will contain a significantly higher concentration of local defects which, along with the better access of substrate molecules due to the higher external specific surface area, will improve the heterogeneous catalytic performances. In addition, nanocrystallites may also be employed as the active chemical photoluminescent entities in the fabrication of composite materials.

4. MATERIALS AND METHODS

4.1. General Instrumentation. SEM (Scanning Electron Microscopy) images and EDS data were collected using either a Hitachi S-4100 field emission gun tungsten filament instrument working at 25 kV or a scanning electron microscope SU-70 working at 4 kV. Samples were prepared by deposition on aluminum sample holders followed by either (i) carbon coating or (ii) Au/Pd coating. The cathodic deposition of the 60% Au/40% Pd metallic alloy was performed using a Polaron Equipment Limited SEM Coating E5000. SEM mapping images and STEM of **1** were recorded using the microscope SU-70 working at 15 or 30 kV, respectively.

TEM (Transmission Electron Microscopy) images were acquired in a HR-TEM Hitachi H9000na. A suspension of **1** in ethanol was sonicated for 180 s. One drop of this suspension was then placed on a carbon-coated copper grid and left in open air to dry. TEM analysis reveals that **1** is extremely sensitive to the electron beam, and under normal conditions, crystallites are destroyed after a few seconds of intense irradiation. To minimize damage, a minimum electron voltage was employed for TEM measurements (200 kV), and the magnification was kept as low as possible.

Thermogravimetric analyses (TGA) were carried out using a Shimadzu TGA 50, from room temperature to ca. 800 °C, with a heating rate of 5 °C/min, under a continuous stream of air with a flow rate of 20 mL/min.

Fourier Transform Infrared (FT-IR) spectra (in the range 4000−500 cm^{-1}) were recorded as KBr pellets (2 mg of sample was mixed in a mortar with 200 mg of KBr) using a Mattson 7000 galaxy series spectrometer equipped with a DTGS CsI detector or using a Bruker Tensor 27 spectrometer by averaging 200 scans at a maximum resolution of 2 cm^{-1}.

Elemental analyses for carbon, nitrogen, and hydrogen were carried out on an LECO CHNS − 932 equipment. Samples were combusted at 1000 °C for 3 min with helium used as the purge gas.

Routine powder X-ray diffraction (PXRD) data for all synthesized materials were collected at ambient temperature on a X'Pert MPD Philips diffractometer, equipped with an X'Celerator detector and a flat-plate sample holder in a Bragg−Brentano para-focusing optics configuration (40 kV, 50 mA). Intensity data were collected by the step-counting method (step 0.04°), in continuous mode, in the ca. $5 \leq 2\theta \leq 50°$ range.

^{13}C CP MAS and ^{31}P spectra were recorded at 9.4 T on a Bruker Avance 400 wide-bore spectrometer (DSX model) on a 4 mm BL cross-polarization magic-angle spinning (CPMAS) VTN probe at 100.6 and 161.9 MHz, respectively. For the ^{13}C CP MAS spectra, the Hartmann−Hahn (HH) "sideband" matching condition $\nu_1^{13C} = \nu_1^{1H} +$

$n\nu_R$ ($n = \pm 1$) was carefully matched by calibrating the ^{1}H and the ^{13}C *rf* field strengths: recycle delay, 5s; contact time, 2 ms; ν_R = 12 kHz. For the ^{31}P spectra, a 90° single pulse excitation of 2.5 μs was employed: recycle delay, 60s; ν_R = 10 kHz. For the ^{31}P CP MAS spectra, a 90° single pulse excitation of 2.5 μs was employed: recycle delay, 5s; contact time, 2 ms; ν_R = 10 kHz. Chemical shifts are quoted in parts per million with respect to TMS for the ^{13}C nuclei and to an 85% H_3PO_4 solution for the ^{31}P nucleus.

4.2. Reagents. Chemicals were readily available from commercial sources and were used as received without further purification: lanthanide (III) chloride hydrates ($LnCl_3 \cdot xH_2O$, $Ln^{3+} = La^{3+}$, Eu^{3+} and Tb^{3+}; at least 99% of purity, Sigma-Aldrich); nitrilotris(methylenephosphonic acid) (H_6nmp, $N(CH_2PO_3H_2)_3$, 97%, Fluka); *n*-hexane puriss *p.a.* (Sigma-Aldrich); styrene oxide (Fluka, ≥97%), ethanol (Panreac, Absolute), methanol (Sigma-Aldrich, 99%).

4.3. Microwave-Assisted Hydrothermal Synthesis. *4.3.1. Typical Preparation of [La(H_3nmp)].* A suspension containing H_6nmp (0.153 g, 0.512 mmol) and $LaCl_3 \cdot 7H_2O$ (0.190 g, 0.512 mmol) in ca. 6.0 mL of distilled water (molar ratios of about 1:1:650) was stirred thoroughly in open air (room temperature) for five minutes. The resulting suspension, with a pH varying between ca. 3 and 5, was transferred to a 10 mL IntelliVent reactor which was placed inside a CEM Focused Microwave Synthesis System Discover S-Class equipment. Reactions took place with constant magnetic stirring (controlled by the microwave equipment) and by monitoring the temperature and pressure inside the vessels. A constant flow of air (ca. 10 bar of pressure) assured a close control of the temperature inside the vessel. After reacting, a white suspension was obtained, and the final product was recovered by vacuum filtration, followed by washing with copious amounts of distilled water, and then air-dried overnight.

CHN elemental composition. Calcd (in %): C, 8.28; H, 2.09; N, 3.22 (C/N = 2.57). Found (in %): C, 7.90; H, 2.12; N, 3.09 (C/N = 2.56).

Thermogravimetric analysis (TGA) data (weight losses in %) and derivative thermogravimetric peaks (DTG; in italics inside the parentheses): 280−400 °C −4.1% (*366 °C*), 400−650 °C −4.8% (*508 °C*), 650−800 °C −4.1% (*768 °C*).

4.3.2. Optimization. The microwave-assisted synthesis conditions to prepare [La(H_3nmp)] (**1**) were investigated by systematically varying the following experimental parameters:

(i) temperature (T) from 120 to 165 °C;
(ii) power (P) from 50 to 100 W;
(iii) reaction time (t) between 1 and 10 min of microwave irradiation.

For simplicity, each sample is identified as $T_mP_nt_p$, as described in the optimization diagram, with the subscripts indicating each set of specifically employed experimental conditions. The set of the prepared materials is depicted in Scheme 1.

4.3.3. Preparation of Mixed-Lanthanide Materials. Mixed-lanthanide compounds having 5% of Eu^{3+} or Tb^{3+} (randomly dispersed in the La^{3+} matrix) were obtained using an experimental procedure similar to that described above while adjusting the stoichiometric amounts of the lanthanide chloride salts to the desired amounts.

4.4. Dynamic Hydrothermal Synthesis. Dynamic hydrothermal syntheses, i.e., with continuous rotation of the vessels during the period of the reaction, have been performed using Teflon-lined autoclaves purchased from Parr Instruments (internal volume of ca. 24 mL) and a custom-modified oven with the internal temperature controlled by an Eurotherm thermostat system.

Reaction mixtures with chemical compositions identical to those described for the microwave-assisted synthesis were stirred thoroughly in open air for a few minutes and then transferred into adapted Teflon-lined Parr Instruments reaction vessels, which were then placed inside a preheated oven. The pH of the initial reactive mixtures varied between ca. 3 and 5. The following experimental conditions were systematically varied to optimize the synthetic conditions:

(i) temperature, 120 and 165 °C;
(ii) speed of rotation, 25 and 50 rpm;
(iii) reaction time, 48 and 72 h;
(iv) chemical composition of the reactive mixtures (ligand/metal/water molar ratios), 1:1:325 and 1:1:650 (total volume of distilled water of ca. 10 mL);
(v) reaction vessel internal volume, 24 and 42 mL.

After reacting, the vessels were allowed to cool slowly to ambient temperature. Products were recovered by vacuum filtration, washed with copious amounts of distilled water, and air-dried, and their crystalline structure was investigated using powder X-ray diffraction. For several combinations of the conditions highlighted above, we found that the isolated products were systematically obtained as physical mixtures of the desired material alongside with other known and unknown products. The overall optimal conditions to isolate [La(H_3nmp)] (**1**) as a phase-pure compound were found to be 165 °C and 48 h of reaction with a speed of rotation of about 25 rpm.

4.5. Structural Determination from Powder X-ray Diffraction. Conventional powder X-ray diffraction data suitable for structural refinements were collected at ambient temperature on a X'Pert MPD Philips diffractometer (Cu $K_{\alpha 1,2}$ X-radiation, λ_1 = 1.540598 Å and λ_2 = 1.544426 Å), equipped with an X'Celerator detector and a flat-plate sample holder in a Bragg−Brentano para-focusing optics configuration (40 kV, 50 mA). Intensity data were collected by the step-counting method (step 0.01°; 500 or 2500 s per step for the as-prepared and calcined materials, respectively), in continuous mode, in the ca. $4 \le 2\theta \le 110°$ range.

The collected powder X-ray diffraction pattern for [La(H_3nmp)] (**1**) and [La(L)] (**2**) (where $L^{3-} = [-(PO_3CH_2)_2(NH)(CH_2PO_2)O_{1/2}-]_n^{3n-}$) were indexed by means of the routines provided with the software program DICVOL04[36] and by employing the first 20 well-resolved reflections (located using the derivative-based peak search algorithm provided with Fullprof.2k)[37] and a fixed absolute error on each line of 0.03° 2θ. Initial unit cell metrics were obtained with reasonable figures-of-merit (see Table 1 for the M[38] and F[39] values).

Analysis of the systematic absences was performed using CHECKCELL[40] which identified the orthorhombic $Pca2_1$ space group as the most suitable. Structure solution was carried out using the direct methods of SIRPOW, included in the software package eXpo2004 (Version 2.1).[41] After subtraction of the background using polynomial functions in selected angular intervals, the intensity of each individual reflection was extracted by employing Pearson profile functions. This strategy allowed the location of most non-hydrogen atoms composing the asymmetric unit, namely, the lanthanide metallic center and the phosphorus atoms. Despite that the powder X-ray diffraction pattern of **1** has a high signal-to-noise ratio, the location of the remaining atoms of the organic molecule proved to be difficult. This was particularly challenging for the calcined material **2**. Initial crystallographic positions were ultimately calculated in eXpo2004 by employing a battery of heavy geometrical constraints for the organic moiety.

Rietveld structural refinement[42] was performed with FullProf.2k[37] by applying fixed background points throughout the entire angular range determined by the linear interpolation between consecutive (and manually selected) breakpoints in the powder pattern. For material **1**, typical pseudo-Voigt profile functions, along with two asymmetry correction parameters, were selected to generate the line shapes of the simulated diffraction peaks. The powder profile of compound **2** could not be adequately simulated by using the same peak shape profile as that used for **1**. Instead, an instrument resolution file has been employed in conjunction with Thompson−Cox−Hastings pseudo-Voigt profiles to generate the line shapes of individual simulated diffraction peaks. This allowed the modeling of each reflection by assuming an anisotropic

broadening due to crystallite size effects. Ylm's up to the fourth order (spherical harmonics) have been employed and refined during Rietveld stages which converged to the values summarized in Table 1. The full-width-at-half-maximum (fwhm) of the Gaussian (H_G) and Lorentzian (H_L) components were refined to $G = 0.0151(4)$ and $L = 3.48(6)$. For both materials, the angular dependence of the individual reflections was also taken into account by employing a Caglioti function correction.[43]

The collected powder pattern of compound **2** was found to exhibit strong preferential orientation along the [010] vector. A modified March's correction function was employed producing refined G1 values of about 0.579(1) (for model I) or 0.654(2) (for model II), which are coherent with the platy crystal habit observed for the material (see SEM inset picture in Figure 6).

Overall structural refinements for the two structures derived from eXpo2004 were performed in consecutive stages to avoid instability and divergence. Zero shift (whenever pertinent), scale factor, parameters related to peak shape, and unit cell parameters were consecutively added as fully refineable variables upon previous full convergence of the remaining parameters to their optimal values. Fractional atomic coordinates for all non-hydrogen atoms were ultimately allowed to refine in conjunction with weighted soft distance constraints solely applied to the H_3nmp^{3-} residue (N−C, C−C, C−P, P−O, and O···O bond lengths and internuclear distances, respectively). This approach, when applied to the as-synthesized [La(H_3nmp)] material, has the advantage of ensuring a final chemically feasible geometry for this organic moiety, while it allows the rare-earth environment to refine freely. For the calcined compound, further restraints associated with the La−O bond lengths were employed. For both structures, each family of atom type has been refined using common refineable isotropic parameters. No correction was made for absorption effects. After full convergence of the model, the hydrogen atoms associated with the $-CH_2-$, −NH, and −POH moieties were placed in the structural model in calculated positions. The final Rietveld refinements were performed with the fractional atomic coordinates of the hydrogen atoms fixed (to avoid divergence), ultimately converging to the profile and reliability factors summarized in Table 1.

Table 1 collects the X-ray data collection, crystal data, and final Rietveld refinement details (profile and reliability factors) for the [La(H_3nmp)] (**1**) and the two models of the [La(L)] (**2**) materials. The final Rietveld plots for **1** and **2** (both models) are supplied in Figures 3 and 6, respectively.

Crystallographic data (excluding structure factors) for the two structures reported in this paper have been deposited with the Cambridge Crystallographic Data Centre as supplementary publication nos. CCDC-818078, -818079, and -836614 (for **1** and model I and II of **2**, respectively). Copies of the data can be obtained free of charge on application to CCDC, 12 Union Road, Cambridge CB2 2EZ, U.K. (fax: (+44) 1223 336033; e-mail: deposit@ccdc.cam.ac.uk).

4.6. Variable-Temperature Powder X-ray Diffraction. Variable-temperature powder X-ray diffraction data for [La(H_3nmp)] were collected on an X'Pert MPD Philips diffractometer (Cu K_α X-radiation, λ = 1.54060 Å), equipped with an X'Celerator detector, a curved graphite-monochromated radiation, a flat-plate sample holder in a Bragg−Brentano para-focusing optics configuration (40 kV, 50 mA), and a high-temperature Anton Parr HKL 16 chamber controlled by an Anton Parr 100 TCU unit. Intensity data were collected in the step mode (0.04°, 15 s per step) in the range ca. $5 \le 2\theta \le 35°$. Data were collected between 30 and 800 °C.

4.7. Photoluminescence. Photoluminescence measurements were recorded on a Fluorolog-3 model FL3-2T with a double excitation spectrometer (Triax 320), fitted with a 1200 grooves/mm grating blazed at 330 nm, and a single emission spectrometer (Triax 320), fitted with a 1200 grooves/mm grating blazed at 500 nm, coupled to an R928 photomultiplier. Excitation spectra were corrected from 240 to 600 nm for the spectral distribution of the lamp intensity using a photodiode reference detector. Emission spectra were corrected for the spectral response of the monochromators and the detector using typical correction spectra provided by the manufacturer. Time-resolved measurements were carried out using a 1934D3 phosphorimeter coupled to the Fluorolog-3, and a Xe−Hg flash lamp (6 μs/pulse half width and 20−30 μs tail) was used as the excitation source. Measurements at 11 K were performed using a He closed-cycle cryostat.

4.8. Heterogeneous Catalysis. A 5 mL borosilicate batch reactor equipped with a magnetic stirrer and a valve for sampling was charged with catalyst **1** (34.7 mg, ca. 0.08 mmol of La^{3+}), alcohol (2 mL), and epoxide (0.83 mmol). The reaction was carried out under atmospheric air and immersed in an external thermostatted oil bath. Screening tests showed that **1** exhibited poor catalytic activity in the oxidative dehydrogenation of alcohols (may take place over basic sites), the epoxidation of olefins (may take place over Lewis acid sites), and the isomerization of α-pinene (may take place over Lewis acid sites), at 55 °C (see Table S1 in the Supporting Information). The evolution of the catalytic reactions was monitored using a Varian 3900 GC equipped with a capillary column (SPB-5, 20 m × 0.25 mm) and a flame ionization detector (using 1-octene as an external standard). Reaction products were identified by GC-MS (Trace GC 2000 Series (Thermo Quest CE Instruments) - DSQ II (Thermo Scientific)), using He as the carrier gas.

■ ASSOCIATED CONTENT

Supporting Information. Additional crystallographic information and studies: crystal structures in CIF format and videos depicting the two models for the in situ condensation reaction which produces the infinite one-dimensional organic ligand. Electron microscopy studies: EDS mapping and quantification of the various elements constituting the mixed-lanthanide materials; TEM studies of the calcined material **2**. Solid-state NMR studies: $^{13}C\{^1H\}$ and $^{31}P\{^1H\}$ CP MAS spectra of [La(H_3nmp)] (**1**) and [La(L)] (**2**). Thermogravimetric studies on compound **2**. Transformation of **1** into **2** accompanied by FT-IR spectroscopy. Additional photoluminescence data. Structural characterization of the reused catalyst **1** in the catalytic experiments reported in the manuscript. Table of all catalytic reactions studied for **1** which did not produce feasible conversions. This material is available free of charge via the Internet at http://pubs.acs.org.

■ AUTHOR INFORMATION

Corresponding Author
filipe.paz@ua.pt

■ ACKNOWLEDGMENT

We are grateful to Fundação para a Ciência e a Tecnologia (FCT, Portugal) for their financial support through the R&D project PTDC/QUI-QUI/098098/2008, for the doctoral research grant No. SFRH/BD/46601/2008 (to PS), and for the postdoctoral research grants Nos. SFRH/BPD/63736/2009 (to JAF) and SFRH/BPD/46473/2008 (to SMB). We further wish to thank FCT for their BII research grants (to FV) programme.

■ REFERENCES

(1) (a) Férey, G. *Chem. Soc. Rev.* **2008**, *37*, 191–214. (b) Rosseinsky, M. J. *Microporous Mesoporous Mater.* **2004**, *73*, 15–30. (c) Rowsell, J. L. C.; Yaghi, O. M. *Microporous Mesoporous Mater.* **2004**, *73*, 3–14. (d) Kitagawa, S.; Furukawa, S. In *Frontiers in Crystal Engineering*; Tiekink,

E. R. T., Vittal, J. J., Eds.; John Wiley & Sons, Ltd: Sussex, 2006, pp 195−263. (e) Kitagawa, S.; Kitaura, R.; Noro, S. *Angew. Chem., Int. Ed.* **2004**, *43*, 2334–2375. (f) Kitagawa, S.; Uemura, K. *Chem. Soc. Rev.* **2005**, *34*, 109–119. (g) Eddaoudi, M.; Kim, J.; Rosi, N.; Vodak, D.; Wachter, J.; O'Keeffe, M.; Yaghi, O. M. *Science* **2002**, *295*, 469–472. (h) Eddaoudi, M.; Moler, D. B.; Li, H. L.; Chen, B. L.; Reineke, T. M.; O'Keeffe, M.; Yaghi, O. M. *Acc. Chem. Res.* **2001**, *34*, 319–330.

(2) (a) Yaghi, O. M.; Li, H. L.; Davis, C.; Richardson, D.; Groy, T. L. *Acc. Chem. Res.* **1998**, *31*, 474–484. (b) Batten, S. R.; Robson, R. *Angew. Chem., Int. Ed.* **1998**, *37*, 1461–1494. (c) Blatov, V. A.; Carlucci, L.; Ciani, G.; Proserpio, D. M. *CrystEngComm* **2004**, *6*, 377–395. (d) Carlucci, L.; Ciani, G.; Proserpio, D. M. *Coord. Chem. Rev.* **2003**, *246*, 247–289.

(3) Mueller, U.; Schubert, M.; Teich, F.; Puetter, H.; Schierle-Arndt, K.; Pastre, J. *J. Mater. Chem.* **2005**, *16*, 626–636.

(4) (a) Chizallet, C.; Lazare, S.; Bazer-Bachi, D.; Bonnier, F.; Lecocq, V.; Soyer, E.; Quoineaud, A. A.; Bats, N. *J. Am. Chem. Soc.* **2010**, *132*, 12365–12377. (b) Dang, D. B.; Wu, P. Y.; He, C.; Xie, Z.; Duan, C. Y. *J. Am. Chem. Soc.* **2010**, *132*, 14321–14323. (c) Fei, H. H.; Rogow, D. L.; Oliver, S. R. J. *J. Am. Chem. Soc.* **2010**, *132*, 7202–7209. (d) Liu, Y.; Xuan, W. M.; Cui, Y. *Adv. Mater.* **2010**, *22*, 4112–4135. (e) Ma, L. Q.; Wu, C. D.; Wanderley, M. M.; Lin, W. B. *Angew. Chem., Int. Ed.* **2010**, *49*, 8244–8248. (f) Corma, A.; Garcia, H.; Xamena, F. X. L. *Chem. Rev.* **2010**, *110*, 4606–4655. (g) Thallapally, P. K.; Fernandez, C. A.; Motkuri, R. K.; Nune, S. K.; Liu, J.; Peden, C. H. F. *Dalton Trans.* **2010**, *39*, 1692–1694. (h) Lee, J.; Farha, O. K.; Roberts, J.; Scheidt, K. A.; Nguyen, S. T.; Hupp, J. T. *Chem. Soc. Rev.* **2009**, *38*, 1450–1459. (i) Ma, L. Q.; Abney, C.; Lin, W. B. *Chem. Soc. Rev.* **2009**, *38*, 1248–1256.

(5) (a) Shimomura, S.; Higuchi, M.; Matsuda, R.; Yoneda, K.; Hijikata, Y.; Kubota, Y.; Mita, Y.; Kim, J.; Takata, M.; Kitagawa, S. *Nat. Chem.* **2010**, *2*, 633–637. (b) Lamia, N.; Jorge, M.; Granato, M. A.; Paz, F. A. A.; Chevreau, H.; Rodrigues, A. E. *Chem. Eng. Sci.* **2009**, *64*, 3246–3259. (c) Choi, H. J.; Dinca, M.; Long, J. R. *J. Am. Chem. Soc.* **2008**, *130*, 7848–7850.

(6) Pereira, G. A.; Peters, J. A.; Paz, F. A. A.; Rocha, J.; Geraldes, C. *Inorg. Chem.* **2010**, *49*, 2969–2974.

(7) (a) Bae, T. H.; Lee, J. S.; Qiu, W. L.; Koros, W. J.; Jones, C. W.; Nair, S. *Angew. Chem., Int. Ed.* **2010**, *49*, 9863–9866. (b) Gascon, J.; Kapteijn, F. *Angew. Chem., Int. Ed.* **2010**, *49*, 1530–1532. (c) Hu, Y. X.; Dong, X. L.; Nan, J. P.; Jin, W. Q.; Ren, X. M.; Xu, N. P.; Lee, Y. M. *Chem. Commun.* **2011**, *47*, 737–739. (d) Huang, A. S.; Dou, W.; Caro, J. *J. Am. Chem. Soc.* **2010**, *132*, 15562–15564. (e) Venna, S. R.; Carreon, M. A. *J. Am. Chem. Soc.* **2010**, *132*, 76–78. (f) Ranjan, R.; Tsapatsis, M. *Chem. Mater.* **2009**, *21*, 4920–4924.

(8) (a) Ameloot, R.; Pandey, L.; Van der Auweraer, M.; Alaerts, L.; Sels, B. F.; De Vos, D. E. *Chem. Commun.* **2010**, *46*, 3735–3737. (b) Lu, G.; Hupp, J. T. *J. Am. Chem. Soc.* **2010**, *132*, 7832–7833. (c) Zacher, D.; Shekhah, O.; Woll, C.; Fischer, R. A. *Chem. Soc. Rev.* **2009**, *38*, 1418–1429. (d) Horcajada, P.; Serre, C.; Grosso, D.; Boissiere, C.; Perruchas, S.; Sanchez, C.; Férey, G. *Adv. Mater. (Weinheim, Ger.)* **2009**, *21*, 1931–1935.

(9) Allendorf, M. D.; Bauer, C. A.; Bhakta, R. K.; Houk, R. J. T. *Chem. Soc. Rev.* **2009**, *38*, 1330–1352.

(10) Seo, J. S.; Whang, D.; Lee, H.; Jun, S. I.; Oh, J.; Jeon, Y. J.; Kim, K. *Nature* **2000**, *404*, 982–986.

(11) (a) Ryu, D. W.; Lee, W. R.; Lee, J. W.; Yoon, J. H.; Kim, H. C.; Koh, E. K.; Hong, C. S. *Chem. Commun.* **2010**, *46*, 8779–8781. (b) Tian, H.; Jia, Q. X.; Gao, E. Q.; Wang, Q. L. *Chem. Commun.* **2010**, *46*, 5349–5351. (c) Tong, X. L.; Hu, T. L.; Zhao, J. P.; Wang, Y. K.; Zhang, H.; Bu, X. H. *Chem. Commun.* **2010**, *46*, 8543–8545. (d) Maspoch, D.; Ruiz-Molina, D.; Wurst, K.; Domingo, N.; Cavallini, M.; Biscarini, F.; Tejada, J.; Rovira, C.; Veciana, J. *Nat. Mater.* **2003**, *2*, 190–195. (e) Roques, N.; Mugnaini, V.; Veciana, J. In *Functional Metal-Organic Frameworks: Gas Storage, Separation and Catalysis*; Springer-Verlag: Berlin, 2010; Vol. 293, pp 207−258. (f) Maspoch, D.; Domingo, N.; Molina, D. R.; Wurst, K.; Hernandez, J. M.; Vaughan, G.; Rovira, C.; Lloret, F.; Tejada, J.; Veciana, J. *Chem. Commun* **2005**, 5035–5037. (g) Maspoch, D.; Ruiz-Molina, D.; Veciana, J. *J. Mater. Chem.* **2004**, *14*, 2713–2723. (h) Maspoch, D.; Ruiz-Molina, D.; Veciana, J. *Chem. Soc. Rev.* **2007**, *36*, 770–818.

(12) (a) Shimizu, G. K. H.; Vaidhyanathan, R.; Taylor, J. M. *Chem. Soc. Rev.* **2009**, *38*, 1430–1449. (b) Taylor, J. M.; Mahmoudkhani, A. H.; Shimizu, G. K. H. *Angew. Chem., Int. Ed.* **2007**, *46*, 795–798. (c) Evans, O. R.; Ngo, H. L.; Lin, W. B. *J. Am. Chem. Soc.* **2001**, *123*, 10395–10396.

(13) Clearfield, A. *Curr. Opin. Solid State Mater. Sci.* **1996**, *1*, 268–278.

(14) Rocha, J.; Carlos, L. D.; Paz, F. A. A.; Ananias, D. *Chem. Soc. Rev.* **2011**, *40*, 926–940.

(15) (a) Harbuzaru, B. V.; Corma, A.; Rey, F.; Atienzar, P.; Jorda, J. L.; Garcia, H.; Ananias, D.; Carlos, L. D.; Rocha, J. *Angew. Chem., Int. Ed.* **2008**, *47*, 1080–1083. (b) Harbuzaru, B. V.; Corma, A.; Rey, F.; Jorda, J. L.; Ananias, D.; Carlos, L. D.; Rocha, J. *Angew. Chem., Int. Ed.* **2009**, *48*, 6476–6479.

(16) Paz, F. A. A.; Klinowski, J. *J. Phys. Org. Chem.* **2003**, *16*, 772–782.

(17) Paz, F. A. A.; Rocha, J.; Klinowski, J.; Trindade, T.; Shi, F. N.; Mafra, L. *Prog. Solid State Chem.* **2005**, *33*, 113–125.

(18) (a) Cunha-Silva, L.; Ananias, D.; Carlos, L. D.; Paz, F. A. A.; Rocha, J. *Z. Kristallogr.* **2009**, *224*, 261–272. (b) Cunha-Silva, L.; Lima, S.; Ananias, D.; Silva, P.; Mafra, L.; Carlos, L. D.; Pillinger, M.; Valente, A. A.; Paz, F. A. A.; Rocha, J. *J. Mater. Chem.* **2009**, *19*, 2618–2632.

(19) Cunha-Silva, L.; Mafra, L.; Ananias, D.; Carlos, L. D.; Rocha, J.; Paz, F. A. A. *Chem. Mater.* **2007**, *19*, 3527–3538.

(20) (a) Li, H. D.; Zhang, L. R.; Li, G. H.; Yu, Y.; Huo, Q. S.; Liu, Y. L. *Microporous Mesoporous Mat* **2010**, *131*, 186–191. (b) Demadis, K. D.; Mantzaridis, C.; Lykoudis, P. *Ind. Eng. Chem. Res.* **2006**, *45*, 7795–7800. (c) Demadis, K. D.; Katarachia, S. D.; Koutmos, M. *Inorg. Chem. Commun.* **2005**, *8*, 254–258. (d) Popov, A.; Ronkkomaki, H.; Popov, K.; Lajunen, L. H. J.; Vendilo, A. *Inorg. Chim. Acta* **2003**, *353*, 1–7. (e) Mao, J.-G.; Wang, Z.; Clearfield, A. *New J. Chem.* **2002**, *26*, 1010–1014. (f) Cabeza, A.; Ouyang, X.; Sharma, C. V. K.; Aranda, M. A. G.; Bruque, S.; Clearfield, A. *Inorg. Chem.* **2002**, *41*, 2325–2333. (g) Sharma, C. V. K.; Clearfield, A.; Cabeza, A.; Aranda, M. A. G.; Bruque, S. *J. Am. Chem. Soc.* **2001**, *123*, 2885–2886. (h) Cecconi, F.; Ghilardi, C. A.; Lorenzo Luis, P. A.; Midollini, S.; Orlandini, A.; Dakternieks, D.; Duthie, A.; Dominguez, S.; Berti, E.; Vacca, A. *Dalton Trans.* **2001**, 211–217. (i) Li, C. Y.; Gao, J. Z.; Yang, W.; Li, B. Y.; Liu, H. T. *Rare Met.* **2000**, *19*, 136–140. (j) Sawada, K.; Kuribayashi, M.; Suzuki, T.; Miyamoto, H. *J. Solution Chem.* **1991**, *20*, 829–839.

(21) Klinowski, J.; Paz, F. A. A.; Silva, P.; Rocha, J. *Dalton Trans.* **2011**, *40*, 321–330.

(22) Smith, J. G. *Synthesis* **1984**, 629–656.

(23) Choi, J. S.; Son, W. J.; Kim, J.; Ahn, W. S. *Microporous Mesoporous Mater.* **2008**, *116*, 727–731.

(24) (a) Ben Akacha, A.; Barkallah, S.; Zantour, H. *Magn. Reson. Chem.* **1999**, *37*, 916–920. (b) Gacs-Baitz, E.; Wozniak, L. A.; Kajtar-Peredy, M. *Chirality* **2000**, *12*, 675–680.

(25) MacKenzie, K. J. D.; Smith, M. E. *Multinuclear Solid-State NMR of Inorganic Materials*; Pergamon: Oxford, 2002; Vol. 6.

(26) Socrates, G. *Infrared Characteristic Group Frequencies - Tables and Charts*; 2nd ed.; John Wiley & Sons Ltd: Baffins Lane, Chichester, 1994.

(27) Shi, F. N.; Cunha-Silva, L.; Ferreira, R. A. S.; Mafra, L.; Trindade, T.; Carlos, L. D.; Paz, F. A. A.; Rocha, J. *J. Am. Chem. Soc.* **2008**, *130*, 150–167.

(28) Krishnamohan Sharma, C. V.; Clearfield, A. *J. Am. Chem. Soc.* **2000**, *122*, 4394–4402.

(29) Gonzales-Platas, J.; Rodriguez-Carvajal, J. *GFourier Program*, Version 04.60, March 2007.

(30) Dorenbos, P. *J. Phys., Condens. Matter* **2003**, *15*, 8417–8434.

(31) Blasse, G.; Grabmaier, B. C. *Luminescent Materials*; Springer-Verlag: New York, 1994.

(32) (a) Dhakshinamoorthy, A.; Alvaro, M.; Garcia, H. *Chem.—Eur. J.* **2010**, *16*, 8530–8536. (b) Kumar, G.; Singh, A. P.; Gupta, R. *Eur. J. Inorg. Chem.* **2010**, 5103–5112.

(33) Jiang, D. M.; Urakawa, A.; Yulikov, M.; Mallat, T.; Jeschke, G.; Baiker, A. *Chem.—Eur. J.* **2009**, *15*, 12255–12262.

(34) Mirkhani, V.; Tangestaninejad, S.; Yadollahi, B.; Alipanah, L. *Tetrahedron* **2003**, *59*, 8213–8218.
(35) Berkessel, A.; Ashkenazi, E.; Andreae, M. R. M. *Appl. Catal., A* **2003**, *254*, 27–34.
(36) Boultif, A.; Louer, D. *J. Appl. Crystallogr.* **2004**, *37*, 724–731.
(37) (a) Rodriguez-Carvajal, J. FULLPROF - A Program for Rietveld Refinement and Pattern Matching Analysis. *Abstract of the Satellite Meeting on Powder Diffraction of the XV Congress of the IUCR*, Toulouse, France, 1990; p 127. (b) Roisnel, T.; Rodriguez-Carvajal, J. WinPLOTR [February 2008] - A Windows Tool for Powder Diffraction Pattern Analysis. Materials Science Forum. *Proceedings of the Seventh European Powder Diffraction Conference (EPDIC 7)*; Delhez, R., Mittenmeijer, E.J., Eds.; 2000; pp 118−123.
(38) Boultif, A.; Louer, D. *J. Appl. Crystallogr.* **1991**, *24*, 987–993.
(39) Louer, D. In *Automatic Indexing: Procedures and Applications, Accuracy in Powder Diffraction II*; Gaithersburg, MD, USA, 1992; pp 92−104.
(40) Laugier, J.; Bochu, B. *CHECKCELL - A Software Performing Automatic Cell/Space Group Determination, Collaborative Computational Project Number 14 (CCP14)*; Laboratoire des Matériaux et du Génie Physique de l'Ecole Supérieure de Physique de Grenoble (INPG): France, 2000.
(41) Altomare, A.; Burla, M. C.; Camalli, M.; Carrozzini, B.; Cascarano, G. L.; Giacovazzo, C.; Guagliardi, A.; Moliterni, A. G. G.; Polidori, G.; Rizzi, R. *J. Appl. Crystallogr.* **1999**, *32*, 339–340.
(42) Rietveld, H. M. *J. Appl. Crystallogr.* **1969**, *2*, 65–71.
(43) Caglioti, G.; Paoletti, A.; Ricci, F. P. *Nucl. Instrum.* **1958**, *3*, 223–228.